



ELSEVIER

Contents lists available at ScienceDirect

International Journal of Heat and Mass Transfer

journal homepage: www.elsevier.com/locate/hmt

Phase separation evaporator using pin-fin-porous wall microchannels: Comprehensive upgrading of thermal-hydraulic operating performance

Xiongjiang Yu^{a,b,*}, Jinliang Xu^{a,*}, Guohua Liu^a, Xianbing Ji^a

^a The Beijing Key Laboratory of Multiphase Flow and Heat Transfer for Low Grade Energy Utilization, North China Electric Power University, Beijing, 102206, P.R. China

^b Department of Energy and Process Engineering, Norwegian University of Science and Technology, Trondheim, 7491, Norway

ARTICLE INFO

Article history:

Received 20 December 2019

Revised 28 August 2020

Accepted 12 September 2020

Keywords:

Microchannels

Boiling heat transfer

Gradient-porous-wall

Phase separation

ABSTRACT

Microchannel evaporator has intrinsic drawback of two-phase flow instabilities with large pressure drop that is induced from bubble blockage in microchannels. Here, we propose a new concept of phase-separation evaporator, in which flow instabilities can be completely suppressed by using gradient pin-fin-porous wall microchannels. The phase-separation concept stems from the self-driven motion of nucleated bubbles from pin-fin region to bare channel region. Vapor bubbles release from porous wall at a high frequency of ~1000 Hz that ensures bare channels not totally wrapped by vapor. Thus, ultra-stable flow and heat transfer can be achieved in a wide range of operating parameters: $T_{in} = 81.9\text{--}92.6\text{ }^{\circ}\text{C}$, $P_{in} = 110.57\text{--}219.77\text{ kPa}$, $G = 112\text{--}264\text{ kg/m}^2\text{s}$, $q = 20.79\text{--}292.82\text{ kW/m}^2$ and $x_{out} = 0.005\text{--}0.318$. Both convective evaporation in bare channels and bubble nucleation in porous walls contribute to enhanced performance. Heat transfer coefficients are not changed as the Bo numbers ranging from 6.91×10^{-5} to 7.44×10^{-4} . This is because when heat flux and/or mass flux is changed, one mechanism is strengthened while the other mechanism is weakened to achieve constant overall heat transfer coefficient. This heat transfer mechanism is different from that in conventional microchannels in which nucleation mechanism dominates at small Bo while convective mechanism dominates at large Bo . With mass fluxes in the range of $112\text{--}264\text{ kg/m}^2\text{s}$, pressure drops are not changed versus mass fluxes at a given heat flux, which are caused by the thermal driving effect in porous walls. Stable heat transfer coefficients and pressure drops ensure flexible selection of running parameters. The evaporator can operate at smaller mass flow rates, as long as dry-out does not occur, it can also operate at larger flow rates without accompanying additional pressure drops.

© 2020 Elsevier Ltd. All rights reserved.

1. Introduction

Microchannel heat exchanger (MHE), which has been developed for decades since 1980s, is efficient for thermal management [1]. MHE with single-phase flow has been widely investigated [2], but it is difficult to maintain uniform temperature along flow length, with a limited heat dissipation [3]. On the contrary, convective boiling in microchannels not only improves the non-uniform temperature distribution, but also increases the maximum heat dissipation [4].

For phase change heat transfer, microchannel usually refer to its hydraulic diameter smaller than the capillary length of a working fluid, under which the bubble confinement number Co is larger than 1. For a two-phase flow, bubbles almost occupy the whole

cross-section of microchannels. Hence, microchannels are easily blocked by bubbles [5]. Besides, the bubble blockage in individual channels may give rise to non-symmetry flow and heat transfer among multi-channels, triggering flow instabilities and critical heat flux, which should be avoided for practical applications [6]. Pressure drop in microchannels is another issue to be concerned, which is influenced by two factors. First, the bubble blockage in channels increases the pumping power [5]. Second, the two-phase mixture increases interfacial area between the two-phases, yielding the rise of energy dissipation for fluid transportation [7].

Boiling in microchannels includes two mechanisms of convective heat transfer and nucleate heat transfer, which are coupled to each other to make the problem complicated. Chen proposed that heat transfer coefficient consists of a macroconvective component and a nucleation-induced micro convection component: $h_{tw} = Fh_{macro} + Sh_{micro}$, where F and S are the Reynolds number factor and suppression factor, respectively [8]. The convective component is important at high mass fluxes or vapor mass qualities,

* Corresponding authors.

E-mail addresses: xiongjiang.yu@ntnu.no (X. Yu), xjl@ncepu.edu.cn (J. Xu).

Nomenclature

A_{film}	thin film heating area (m ²)
A_c	effective cross section area of the microchannel (m ²)
$A_{c,f}$	cross section area of single pin fin (m ²)
A_m	oscillation amplitude (m)
$A_{m,l}$	oscillation amplitude in less vapor condition (m)
$A_{m,m}$	oscillation amplitude in more vapor condition (m)
A_{ub}	total bottom area of the unit cell (m ²)
A_{uc}	projected area of pin fins of the unit cell (m ²)
A_{ufin}	total side area of pin fins (m ²)
Bi	Biot number, $Bi = h_1 \delta_{\text{unit}} / k_l$
Bo	dimensionless boiling number, $Bo = q / (h_{\text{fg}} G)$
C_p	specific heat (J/kg K)
D	hydraulic diameter (m)
f	dominating frequency (Hz)
G	mass flux (kg/m ² s)
h	specific enthalpy (kJ/kg)
h_{BCA}	heat transfer coefficient of bare channel area (kW/m ² K)
$h_{c, \text{PFWA}}$	convective heat transfer coefficient of PFWA (kW/m ² K)
h_{fg}	latent heat of evaporation (kJ/kg)
$h_{f, \text{sat}}$	saturation liquid enthalpy (kJ/kg)
h_{in}	inlet liquid enthalpy (kJ/kg)
h_1	local heat transfer coefficient (kW/m ² K)
$h_{n, \text{PFWA}}$	nucleate heat transfer coefficient of PFWA (kW/m ² K)
h_{PFWA}	heat transfer coefficient of pin fin wall area (kW/m ² K)
h_{tp}	two phase heat transfer coefficient (kW/m ² K)
i	number of bare channel
k_1	heat conductivity of water (W/m K)
k_s	heat conductivity of silicon chip (W/m K)
L	characteristic length (m)
l	fluid local position (m)
l_{unit}	length of unit cell (m)
l_{mc}	microchannel length (m)
l_{sp}	liquid phase flow length (m)
m	mass flow rate (kg/s)
Nu	Nusselt number, $Nu = \frac{q}{T_{w,l} - T_{f,l}} \times \frac{D}{k_l}$
n	number of samples
n_{fin}	number of pin fins of unit cell
P	pressure (Pa)
P_{fin}	cross-section perimeter of a single pin fin (m)
ΔP	pressure drop across the microchannel (Pa)
Q	effective heating power (W)
Q_t	heat power (W)
q	effective heat flux (W/m ²)
R_s	standard resistance (Ω)
T	temperature ($^{\circ}\text{C}$)
$T_{f,l}$	local fluid temperature ($^{\circ}\text{C}$)
$T_{w,l}$	local wall temperature ($^{\circ}\text{C}$)
$T_{X,Y}(t)$	wall temperature at the location (X,Y) at time t ($^{\circ}\text{C}$)
$\bar{T}_{X,Y}$	time averaged temperature at (X,Y) ($^{\circ}\text{C}$)
t_1, t_2	time (s)
V_1	voltage on film heater (V)
V_2	voltage on standard resistance and film heater (V)
V_{vacuum}	vacuum volume in the microchannel region (m ³)
v_x	main flow velocity (m/s)
v_y	velocity in channel width direction (m/s)
W	bare channel width (m)

W_{ch}	total width of microchannel heat exchanger (m)
W_{fin}	edge length of pin fin cross section (m)
w	bubble width (m)
w_{unit}	width of unit cell (μm)
X	length along flow direction (mm)
x	vapor mass quality
Y	length along width direction (mm)

Greek symbols

δ_c	etched channel depth (m)
δ_{unit}	thickness of unit cell (m)
η	bubble confinement ratio
η_{fin}	fin efficient
ρ	density (kg/m ³)
ρ_l	liquid density (kg/m ³)
ρ_m	mean fluid density (kg/m ³)
ρ_v	vapor density (kg/m ³)
ω	angular frequency (rad/s)
$\sigma(X, Y)$	standard deviation at position (X,Y)
τ	fluid residence time (s)
φ	thermal efficiency

Subscripts

ave	average
f	liquid
g	vapor
i	number of channels
in	inlet
max	maximum
min	minimum
out	outlet
r	residence
sat	saturated
sp	liquid phase
tp	two phase
w	wall

but the nucleation component is dominant at low mass fluxes or vapor mass qualities. Table 1 summarizes some studies on boiling in microchannels [9–19]. Earlier studies show that annular flow is the dominant flow pattern, hence they conclude thin film evaporation as the dominant heat transfer mechanism, in which the liquid film separates superheating wall and saturation liquid [9–11]. Alternatively, Kandlikar compared bubble dynamics during pool boiling and boiling in confined channels, and emphasizes the importance of nucleation mechanism in microchannels [12]. Based on experiments, Xu and co-authors provide a link between heat transfer mechanisms and flow patterns using Bo number [13]. They conclude that the nucleate mechanism and nucleation mechanism are dominant in low and high Bo ranges, respectively, supporting the Chen's assumption [8]. Until recently, many investigations still comment on boiling mechanisms in microchannels with various working fluids and operating parameters [14–19]. Cheng and Xia summarised investigations on boiling in microchannels, concluding that a general correlation for heat transfer prediction does not exist [20]. Various parameters such as heat flux, mass flux and pressure influence boiling heat transfer in microchannels.

Boiling in microchannels may trigger flow instabilities, including static and dynamic ones [21–23]. The former occurs when the slope of the demand hydraulic curve smaller than that provided by external pumping system [24]:

$$\frac{\partial \Delta P}{\partial G} \Big|_{\text{demand}} \leq \frac{\partial \Delta P}{\partial G} \Big|_{\text{external}} \quad (1)$$

Table 1
Microchannel flow boiling heat transfer studies in the literature.

Reference	micro-condenser test section	working fluid	dominating heat transfer mechanism	comments on two phase heat transfer coefficients
Lee & Lee (2001) [9]	3 single stainless steel rectangular channels: 20 mm wide 0.4, 2 and 2 mm deep	R-113	forced convective boiling	h_{tp} increased with increasing x for $x > 0.15$ and almost independent of q .
Hestroni et al. (2002) [10]	21 parallel silicon triangular channels, $D = 130 \mu\text{m}$	Vertrel XF	forced convective boiling	h_{tp} decreased with increasing x and q , or decreasing G .
Qu & Mudawar (2003) [11]	21 parallel oxygen-free copper rectangle channels: $231 \times 713 \mu\text{m}$	water	forced convective boiling	h_{tp} decreased with increasing x , increase with increasing G .
Kandlikar (2004) [12]	-	-	nucleate boiling	Bubble nucleate, rapid evaporation, flow reversal were similar with the nucleate boiling ebullition cycle.
Xu et al. (2005a) [13]	parallel silicon triangular channels, $D = 154 \mu\text{m}$	acetone	nucleate boiling and forced convective boiling	In low Bo region, h_{tp} increased with increasing q , not sensitive to G ; In high Bo region, h_{tp} increased with increasing G , not sensitive to q .
Kosar et al. (2005) [14]	5 parallel silicon rectangular channels, $D = 227 \mu\text{m}$	water	nucleate boiling and forced convective boiling	High Boiling number and Reynolds number have promoted convective boiling, while Nucleate Boiling dominated at low Reynolds number and Boiling number.
Agostini et al. (2008) [15]	67 parallel silicon channels: $223 \times 680 \mu\text{m}$	R236fa	nucleate boiling	h_{tp} increased with heat flux and was almost independent of vapor quality and mass velocity
Bertsch et al. (2008) [16]	17 parallel copper rectangular channels, $D = 1.09 \text{ mm}$	HFC-134a	-	h_{tp} varied significantly with refrigerant inlet quality and mass flow rate, but only slightly with saturation pressure.
Deng et al. (2014) [17]	14 parallel porous wall copper channels, $D = 786 \mu\text{m}$	deionized water	nucleate boiling and forced convective boiling	Nucleation boiling governed at low heat fluxes, forced convective boiling associated with thin film evaporation dominated at moderate to high heat fluxes.
Falsetti et al. (2017) [18]	parallel silicon channels with pin fin structure, channel width $W_{ch} = 100 \mu\text{m}$	R236fa	-	h_{tp} depended on vapor quality, mass flux and heat flux.
Fayyadh et al. (2017) [19]	25 parallel oxygen free copper rectangular channel, $D = 420 \mu\text{m}$	R134a	nucleate boiling	h_{tp} depended strongly on heat flux while it is a weak function of mass flux.

Specially, for constant pressure driving flow, $\frac{\partial \Delta P}{\partial G} |_{external} = 0$ yields an unstable flow at negative slope of the demand hydraulic curve.

Boiling may trigger pressure drop instability, density wave instability and thermal instability, belonging to dynamic ones. These instabilities are more serious in microchannels than in large size channels, due to flowing reasons: (i) enlarged instabilities due to bubble blockage in microchannels [25]; (ii) intensified density wave propagation due to multi-channels effect; and (iii) significantly large upstream compressible volume relative to microchannels volume enhances pressure drop instability [26–28]. Various techniques such as inlet restrictions [29,30], nucleation cavities [31], diverging channels [32], injection of seed bubbles [33], active inlet flow supply [27], porous walls [34], elongated channel length and enhanced thermal conduction in axial direction [35], were proposed to suppress flow instabilities. In summary, microchannels provide large surface to volume ratio for heat transfer enhancement. However, it possesses drawbacks such as serious vapor blockage and flow instability, which should be overcome for practical applications.

Heat exchanger with phase separation concept was awarded by US patent, referring to gas (vapor) and liquid phases transported in separated flow paths using in-situ separation of the two phases. The first paper regarding condenser tube using phase separation technique was published in 2012 [36]. A membrane separator using mesh screen material is suspended in a condenser tube, generating an annular region and a core region interfaced by the membrane surface. In such a way, liquid flows inside the core region, but vapor flows in the annular region to yield ultra-thin liquid film for heat transfer enhancement. Subsequently, comprehensive investigations on the phase separation tube condenser were conducted, including both experimental and numerical works under different conditions [37–40]. Yu et al. [7] extended the phase separation

concept to micro-condenser using lined pin-fin structure as the in-situ separator. The micro-condenser was fabricated by MicroElectroMechanicalSystem (MEMS) technique, not only enhancing heat transfer due to thin liquid film thickness, but also reducing pressure drops due to decreased interfacial area between the two-phases.

The phase separation concept is also useful for boiling heat transfer. Xu et al. [41] experimentally studied pool boiling using modulated porous structure as the enhanced surface. Small pores in micron scale creates large capillary force for liquid suction, while large pores ($\sim 10 \mu\text{m}$) act as vapor channels for vapor escaping and liquid film evaporation. Jaikummar and Kandlikar [42] conducted experiments using open microchannels with selective sintering on different regions, generating liquid supply passage and vapor removal passage. Such device involves two types of bubbles induced liquid jet enhancement mechanisms. Falzeli et al. [43] covered finned evaporator with a hydrophobic membrane to lock liquid in the evaporator but allow vapor escaping. They showed significantly increased heat removal capacity at high wall superheating. Dai et al. [44] developed a flow separation technique and experimentally demonstrated significantly improved performance of pressure drop and heat transfer. Bai et al. [45] used porous artery structure to provide individual flow paths for liquid supply and vapor venting, avoiding the counter-current flow between the two-phases to raise critical heat flux for pool boiling. In addition to experiment investigations, theoretical and numerical works were also performed in porous channels focusing on local thermal non-equilibrium effect [46], heat transfer performance [47,48] and geometry optimization of porous fins [49].

In this paper, boiling in a phase separation evaporator with pin-fin porous walls was investigated, dividing the cross-section into bare channels area (BCA) and pin-fin porous wall area (PFWA). The gradient porous structure ensures bubbles generated in porous me-

dia automatically releasing into bare channels driven by surface energy, creating bubbles jet in evaporator width direction. An overall thermal performance of the evaporator depends on the contributions from the two regions of PFWA and BCA. We show that at smaller Bo number, convective mechanism in BCA is strong but nucleate mechanism in PFWA is weak. On the other hand, at larger Bo number, nucleate mechanism in PFWA is strong but convective mechanism in BCA is weak. Hence, the overall heat transfer coefficients are insensitive to running parameters. Moreover, pressure drops across microchannels are found to be not sensitive to mass fluxes, exhibiting "flat" hydrodynamic demand curves in two-phase regions to eliminate static instability. Compared with traditional microchannels, the phase-separation evaporator is attractive for performance improvement.

2. Material and methods

2.1. Gradient-porous-wall microchannels

Silicon substrate has a size of 32.0 mm in length, 10.5 mm in width and 400 μm in thickness. The etched substrate was bonded with a 7740 glass to form the whole chip that includes the etched microchannels, inlet and outlet rectangular holes for plenums and a deposited platinum film heater on the back wall (Fig. 1(a)). The microchannels occupy a length of 20.0 mm and a total width of 5500 μm with an etched depth of 75 μm , as showed in Fig. 1(b). The bare channel had a width of 164 μm with a 336 μm width of porous-pin-fin wall and, respectively. Each pin fin had a cross section size of 15 $\mu\text{m} \times 15 \mu\text{m}$ with a dense or a sparse fin-gap of 5 μm and 15 μm , respectively. Fig. 1(c) presents a high-resolution optical image of the resulting gradient-porous-walls for more details. The back-platinum heater is about 300 nm, and its size was exactly correspondence to the microchannel area. Two gold pads were populated at margins of the platinum heater. The electrical resistance of the heater is 64.8 Ω at 24 $^{\circ}\text{C}$. To recognize the local positon, a planar coordinate was established with the origin point (0, 0) located at a corner of the microchannels (Fig. 1(a)). The X and Y coordinates guide to the horizontal (flow direction) and longitudinal direction, respectively.

2.2. Experimental setup

The experimental setup consists of a flow loop and a measurement system, as shown in Fig. 2. The pressurized nitrogen bottle was used to drive the working fluid (pure deionized water). The deionized water flowed through a 7 μm filter before entering a mass flow mete. A needle valve installed at the downstream of the flow meter was used to adjust the flow rate. Then, the working fluid flowed through a hot water bath running at a constant temperature to preheat for achieving a desired inlet temperature. A 3 μm filter was further arranged at the upstream of test chip to prevent impurities entering the microchip. A direct current power was applied to heat the test section. The releasing vapor-liquid flow was cooled by a cold-water bath after discharging from the test section and finally collected by a beaker.

The measurement system includes a high-speed camera (IDT Motion pro Y4, USA) coupled with a microscope, an IR image system (Infrared Camera Image IR 5300 Series, Germany) and a data acquisition system (Yokogawa DL850, Japan). The camera system has a spatial resolution of 1280 pixels by 1024 pixels with a maximum frequency of 58,000 frames per second. The recording rate of 5000 frames per second was used to capture the flow patterns in this study. The IR camera with a micro-lens was placed below the test section to capture the temperature field on the backside of chip. The viewed area was identical to the microchannel area

with a spatial resolution of 91 pixels by 25 pixels. The spatial resolution was about 220 μm per pixel. Hence, the temperature of any point on the heater can be extracted from the thermal image. A thin black lacquer having emissivity of 0.99 was painted on the heater to ensure the measure accuracy. After a careful calibration of the emissivity, temperature accuracy of the black lacquer approaches to 0.5 $^{\circ}\text{C}$. The recording rate of IR image system is 500 samples per second.

The flow rate of working fluid was monitored and acquired by a Coriolis mass flow meter (DMF-1-1AB), with an accuracy of 0.5% and response time of 0.1 s. The pressure transducer and differential pressure transducer (Rosemount 3051) were used to collect pressure data at the inlet and the stride across of the test section, respectively. The transducers had an accuracy of 0.1% with response time of 0.1 s. The inlet and outlet fluid temperatures of the test section were measured by K type thermocouples (Omega) with accuracy of 0.2 $^{\circ}\text{C}$ and response time of 0.2 s. The recording rates of these data were 500 samples per second. Table 1 summarizes detailed information that includes instruments, ranges and uncertainties of the measured parameters.

2.3. Experimental procedures

Before the experiment, a vacuum pump was used to vacuum the whole system and non-condensable gas was degassed from the working fluid. Then, the degassed deionized water was filled into the water tank. The data acquisition system and the optical system were available in waiting mode. A synchronization hub synchronized the measurement equipment during the experiment, and thus all the data are recorded simultaneously including temperatures, pressures, flow rates, input heating power as well as the visualized images. The recording systems start to run after the mass flux and the inlet temperature of the water reaching to steady state.

2.4. Data reduction

Heat flux:

$$q = Q/A_{\text{film}} \quad (2)$$

where $Q = \varphi(V_2 - V_1) \frac{V_1}{R_s}$ is the effective heating power, $V_2 - V_1$ is the applied voltage on the film heater. V_1/R_s is the flowing current and φ is the thermal efficiency of 0.93. φ was determined by the signal phase energy balance, $\varphi = mC_p(T_{\text{out}} - T_{\text{in}})/Q_t$, where m is single-phase mass flow rate, C_p is the specific heat of water, Q_t is the heat power recorded by the power meter.

Mass flux:

$$G = m/A_c \quad (3)$$

where m is the total mass flow rate, A_c is an effective cross section area of the microchannel network and defined as $A_c = \frac{V_{\text{vacuum}}}{l_{\text{mc}}}$, V_{vacuum} is the vacuum volume in the microchannel region excluding all the pin fin volume, l_{mc} is the microchannel length.

Outlet vapor mass quality:

$$x_{\text{out}} = \frac{h_{\text{in}} + \frac{Q}{m} - h_{f,\text{sat}}}{h_{fg}} \quad (4)$$

where h_{in} , $h_{f,\text{sat}}$ and h_{fg} are the inlet water enthalpy, saturation water enthalpy and latent heat of evaporation.

Axial flow velocity:

$$v_x = \frac{G}{\rho_m} \quad (5)$$

where $\rho_m = \rho_v\alpha + \rho_l(1 - \alpha)$ is mean fluid density of two-phase flow, ρ_v is vapor density, ρ_l is liquid density, α is void fraction.

Local heat transfer coefficient:

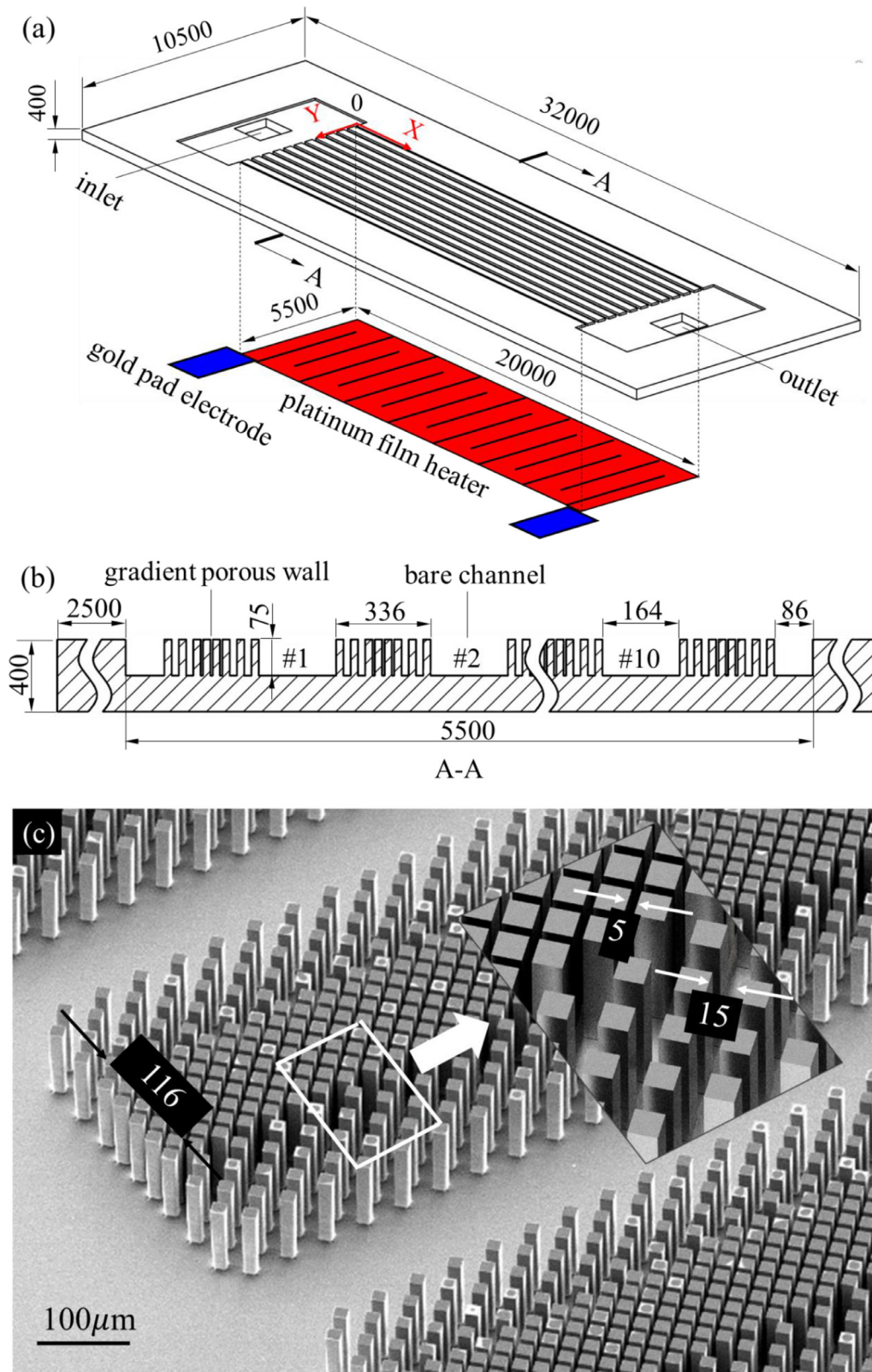


Fig. 1. Porous wall microchannels (a for overall size of the microchannel chip; b for cross section of A-A; c for SEM image of the gradient porous wall).

Due to the geometric symmetry, an area with a width of $500\mu\text{m}$ covering two half bare channels and one single pin-fin porous wall is selected as a unit cell. A simple energy balance equation was applied to a unit cell at $X = l$ that contains both micro-pin fins as well as the surrounding base surface. By assum-

ing heat flux and wall temperature are spatially uniform in the unit cell because of the ultra-small Bi number of silicon base, one can get:

$$qA_{ub} = h_l(T_{w,l} - T_{f,l})(A_{ub} - A_{uc} + \eta_{fin}A_{ufin}) \quad (6)$$

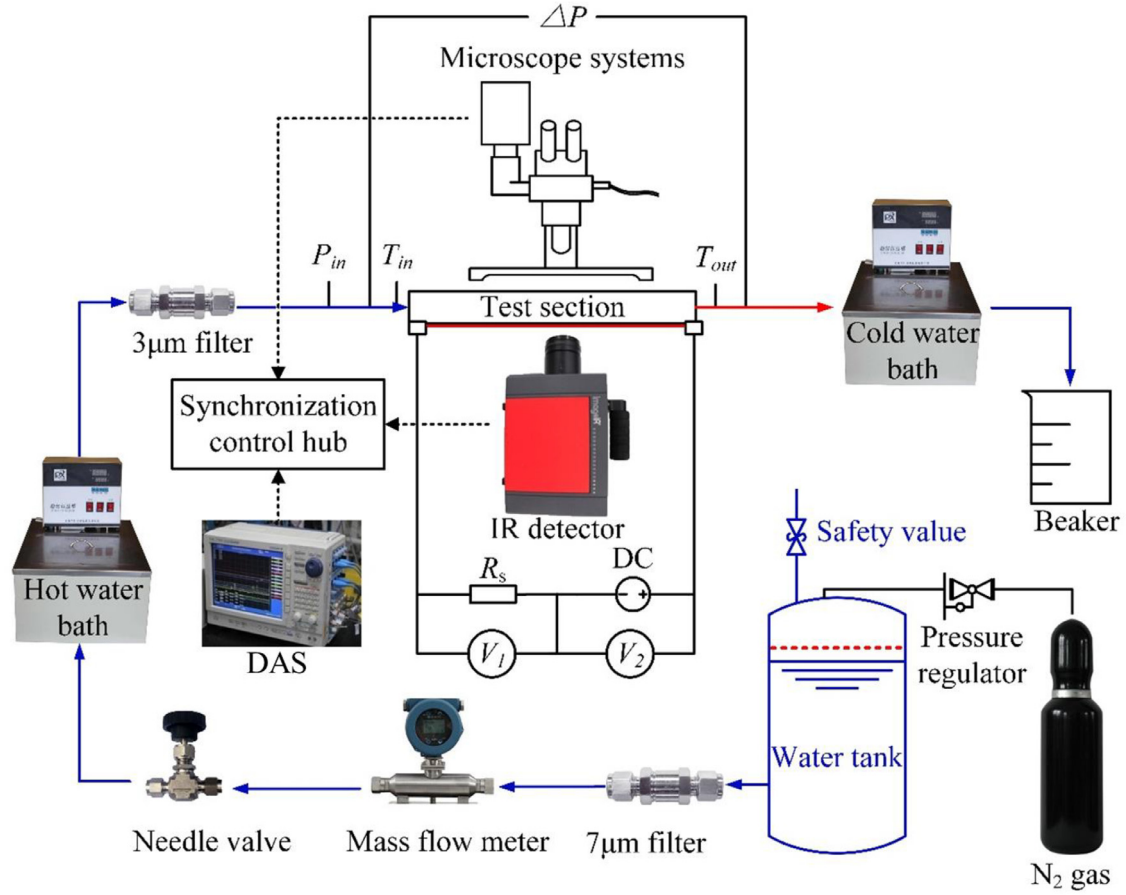


Fig. 2. The experimental setup.

Where $A_{ub} = w_{unit}l_{unit}$ is total bottom area of the unit cell. w_{unit} and l_{unit} are the width and length of the unit cell, respectively. h_1 is local heat transfer coefficient at $X = l$, $T_{w,l}$ is local wall temperature and $T_{f,l}$ is local fluid temperature. $A_{uc} = n_{fin}W_{fin}^2$ is the projected area of pin fins, n_{fin} is the number of pin fins. W_{fin} is the edge length of pin-fin cross section. $A_{ufin} = n_{fin}P_{fin}H$, is total side area of pin-fins. P_{fin} is the cross-section perimeter of a single pin fin. The fin efficient can be calculated by:

$$\left\{ \begin{aligned} \eta_{fin} &= \frac{\tanh(m_{fin}H)}{m_{fin}H} \\ m_{fin} &= \sqrt{\frac{h_1 P_{fin}}{k_s A_{c,f}}} \end{aligned} \right. \quad (7)$$

where k_s is the conductivity of silicon chip, $A_{c,f}$ is the cross section area of single pin-fin. The local fluid temperature at $X = l$ can be calculated by:

$$T_{f,l} = \begin{cases} T_{in} + l \cdot \frac{T_{ONB} - T_{in}}{l_{sp}}, & 0 < l \leq l_{sp} \\ T_{sat,l}(P_{sat,l}), & l_{sp} < l \leq l_{mc} \end{cases} \quad (8)$$

where T_{ONB} is local fluid temperature at the onset of nucleate boiling (ONB), and $P_{sat,l}$ can be calculated by assuming a linear decrease in local pressure in two phase region. Due to ultra-small Bi number ($\sim 10^{-2}$) of silicon base and advantage of untouched temperature measurement of IR, the location ONB is obtained where the axial highest wall temperature is detected. This is because the single-phase fluid temperatures are evidently increasing along flow direction while single-phase heat transfer coefficients do not change much before ONB, leading to the increase of wall temperatures. After ONB, however, sharp increase of heat transfer coefficient occurs owing to boiling heat transfer taking place and

the saturated fluid temperatures decrease with decreasing saturated pressures along channels, leading to the decrease of wall temperatures. Thus, the location of ONB is acquired where highest wall temperature appears. Single phase length l_{sp} can be thereby defined by the distance between channel inlet and the location where highest temperature detected, which can be directly measured by IR camera. In previous papers, single phase length is often calculated according to energy balance. There are two reasons for that: a) Flow instabilities gain troubles for the determination of ONB using characteristic of wall temperatures; b) In case that thermal couples being used to measure temperatures, it is difficult to achieve successive measurement of wall temperatures. In this work, however, the above two shortcomings has been overcome by stable operation and successive temperature measurement of IR, making accurate determination of ONB location available.

The pressure drop along flow direction can be divided into two regions: single phase region and two-phase region. In single phase region, the pressure drop can be expressed as:

$$\Delta P_{sp} = f \cdot \frac{l_{sp}}{D} \cdot \frac{G^2}{2\rho_l} \quad (9)$$

Where f is single phase friction parameter, which is related to Re number of single-phase flow. ρ_l is liquid density. D is hydro diameter of a channel. In order to calibrate the value of f , single phase experiments with different inlet fluid temperatures and mass fluxes were performed. Finally, the single-phase pressure drop part of flow boiling case is calculated using following iterative

calculation adapting the correlation between f and $Re_{l,ave}$:

$$\begin{cases} T_{ONB} = f_1(P_{ONB}) \\ T_{l,ave} = \frac{T_{in} + T_{ONB}}{2} \\ \mu_{l,ave} = f_2(T_{l,ave}) \\ f = f(Re_{l,ave}) \\ \Delta P_l = fT \frac{l_{sp}}{D} \cdot \frac{G^2}{2\rho l} \\ P_{ONB} = P_{in} - \Delta P_l \end{cases} \quad (10)$$

Where P_{ONB} is local pressure of ONB, $\mu_{l,ave}$, $T_{l,ave}$, $Re_{l,ave}$ are average dynamic viscosity, temperature and Reynolds number of single phase flow, respectively. f , f_1 , f_2 are relationships between Reynolds number and single-phase fraction parameter, saturated pressures and temperatures, fluid temperatures and dynamic viscosities, respectively. All the properties and f_1 , f_2 relationships are from NIST 9.1 software. The calculation of local pressure in two-phase region is extremely complicated in present gradient porous wall microchannels not only because the existing of porous media but also because of the “thermal driving” effect which will be discussed later. Thus, a simple linear decrease of local pressure along microchannel in two-phase region was used.

Local Nusselt number (Nu):

$$Nu = \frac{q}{T_{w,l} - T_{f,l}} \times \frac{D}{k_l} \quad (11)$$

where k_l is the thermal conductivity of water.

Totally 59 runs were performed in the present experiment covering the data ranges: $T_{in} = 81.9\text{--}92.6$ °C, $P_{in} = 110.57\text{--}219.77$ kPa, $G = 112\text{--}264$ kg/m²s, $q = 20.79\text{--}292.82$ kW/m², $x_{out} = 0.005\text{--}0.318$. Table 2 listed uncertainties of key parameters. Uncertainties of these parameters were evaluated based on the error transmission theory [50].

3. Fundamental concept of phase separation

3.1. Phase-separation theory

Fig. 3 shows phase separation process under less vapor conditions (see Fig. 3a-c) and more vapor conditions (see Fig. 3d-f). In Fig. 3a, one bubble nucleates at the edge of PFWA, a dash line connecting corners of neighbouring pin fins separates the bubble into up part having spreading length of l_1 and down part having spreading length of l_2 . The contact angles between water and solid silicon surface are measured to be 66.8°. It can be proved theoretically that when l_1 increases, the surface energy of whole three phase system decreases. That means once a bubble is formed at edge of pin fin wall, it will be driven to bare channel due to surface energy gradient as Fig. 3b showed. Finally, the bubble detaches solid pin fins and goes into bare channel by shearing stress of liquid flow as well as further decreasing surface free energy. Fig. 3c shows the bubble completely goes into the bare channel. When there is more vapor in bare channels, the formation and motion of nucleate bubble could push the central vapor core aside (see Fig. 3d-e), owing to releasing of extra local pressure through porous pin-fin walls to other-side channels. After the bubble contacting vapor core and finally merging itself into the vapor flow, shown in Fig. 3f, the surface free energy as well as vapor-liquid interface area become minimum. Thus, boiling phase-separation process is completing.

A bubble-pin-fin system including a half bubble are indicated in Fig. 4. The gas-liquid interface was marked in red color, solid-liquid interface was marked black color.

Gibbs free energy of a system is: $G_{Gibbs} = A_{sg}\gamma_{sg} + A_{lg}\gamma_{lg} + A_{sl}\gamma_{sl}$ where γ is the surface tension, A is the interface area, the subscripts s , g and l represent solid, gas and liquid, respectively. For the problem studied in Fig. 4, $A_{sg}=0$, A_{sl} equals to total side area of

Table 2
The major parameters, instruments and uncertainties.

Parameter	Explanations	Measurements	Uncertainty or relative error
A_c	effective cross section area of the microchannel	determined by MEMS fabrication technique	0.01%
A_{film}	thin film heating area	Chemical vapor deposition	0.01%
G	mass flux	Coriolis mass flow meter (DMF-1-1AB)	0.50%
h_1	local heat transfer coefficient	calculated by Eq. (6)	0.54% ~ 5.46%
w	bubble width	Pixel ruler	±4 μm
W	bare channel width	Physical Vapor Deposition	0.01%
ΔP	pressure drop across the microchannel	Pressure transducer (Rosemount-3051)	0.10%
P_{in}	inlet pressure of the microchannel	Pressure transducer (Rosemount-3051)	0.10%
Q	total heating power	Voltage module(Yokogawa DL750)	±0.12 W
q	effective heat flux	determined by power measurements	±1.1 kW/m ²
$T_{X,Y}(t)$	wall temperature at the location (X,Y) at time t	IR detector(Infra TecImageIR 5300)	Sensitivity of 0.02 °C, accuracy of 0.2 °C, response time of 1 ms.
T_{in}, T_{out}	inlet and outlet flow temperature	K-type thermocouples	0.2 °C

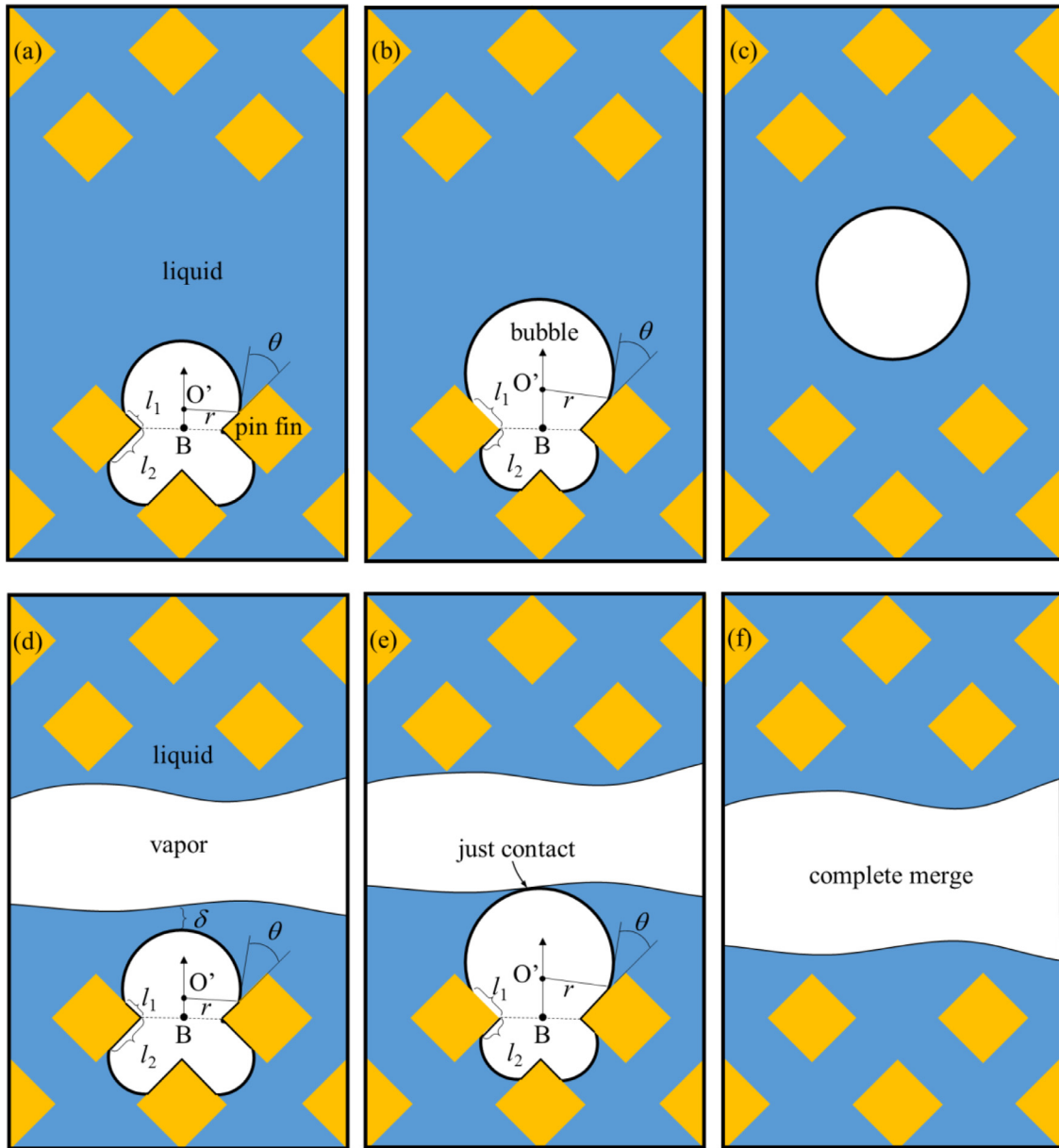


Fig. 3. Surface energy induced phase separation phenomenon: (a for a bubble nucleate in less vapor condition; b for a bubble escapes from PFWA due to decreasing surface energy; c for a bubble detach solid pin fins completely; d for a bubble nucleate in more vapor condition; e for a bubble contact with vapor core and f for the bubble merges itself into the vapor flow after escaping from PFWA.).

pin fins which is a constant. $A_{lg}=H(C_1+l_1+2l_2+C_2)$, where H is the height of pin fins, C_1, l_1, l_2, C_2 are lengths indicated in Fig. 4, noting that all in unit of micro meter. $\theta = 66.8^\circ, \alpha = 135^\circ - \theta = 68.2^\circ, r_0 = \frac{AB}{\sin\alpha} = 11.42$.

Triangle COA is similar with triangle CO'A':

$$\frac{r}{r_0} = \frac{CA'}{CA} = \frac{l_1 + 15}{15} \quad (12)$$

In sector OA'F, differential area with respect to r is written as:

$$dS_{OA'F} = \alpha r \cdot dr \quad (13)$$

In shape ADEC, differential area with respect to l_2 is:

$$dS_{ADEC} = AC \times dl_2 = 15 \cdot dl_2 \quad (14)$$

Assuming constant volume during the bubble moving, we can get:

$$dS_{OA'F} + dS_{ADEC} = 0 \quad (15)$$

By combining (12–15), yields the equation:

$$\frac{dl_2}{dl_1} \approx -0.7 \times \left(\frac{l_1}{15} + 1 \right) \quad (16)$$

It should be noticed that if the down part of the bubble can reach the below pin fin 2, the following equation should be satisfied: $l_1 > 7.15 \mu\text{m}$ according to geometric features. Differentiating G_{Gibbs} with respect to l_1 yields

$$\frac{\partial G_{Gibbs}}{\partial l_1} = \frac{\partial H(C_1 + l_1 + 2l_2 + C_2)\gamma_{lg}}{\partial l_1} = H\gamma_{lg}(0.5 - 0.1l_1) \quad (17)$$

Under condition that $l_1 > 7.15 \mu\text{m}$, $\frac{\partial G_{Gibbs}}{\partial l_1} < 0$, indicating the surface free energy of whole three phase system decreases when l_1 increases.

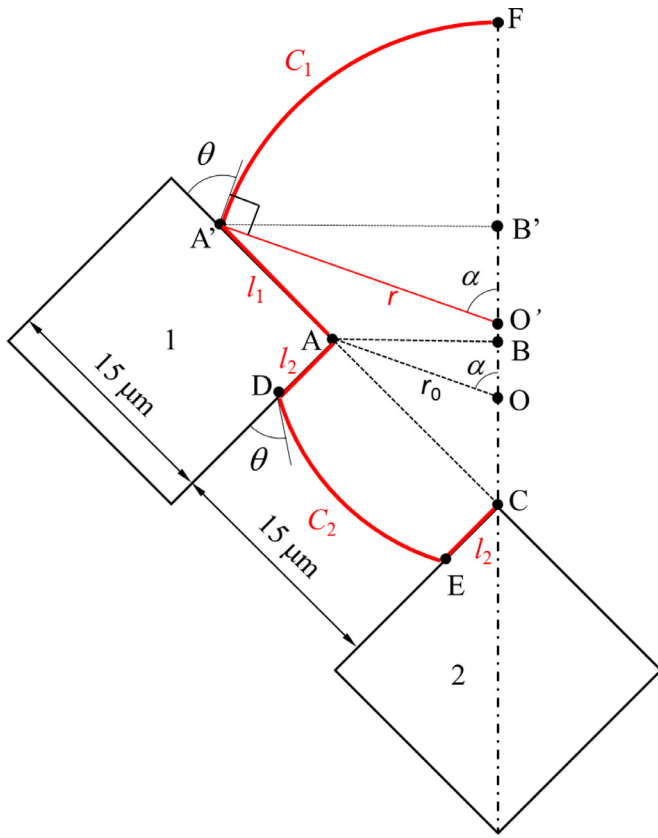


Fig. 4. Gibbs free energy analysis of growing bubble at interface between PFWA and BCA.

3.2. Mass exchange

Fig. 5 illustrates pressure-delivering process between neighbouring channels. At $t = t_1$, local pressure in down channel is high due to bubble expanding, imbalanced pressure pushing the bubble in up channel away from porous wall, leaving more space to liquid to pass through. The pressure difference between two channels can be expressed as [34],

$$P_{f,i} - P_{f,i+1} = \rho_g R (T_{g,i} - T_{g,i+1}) - \left\{ m_{e,i}^2 \left[\frac{\rho_f - \rho_g}{\rho_f \rho_g} \right]_i - m_{e,i+1}^2 \left[\frac{\rho_f - \rho_g}{\rho_f \rho_g} \right]_{i+1} \right\} \quad (18)$$

where P , R , T , m_e , ρ , are pressure, density, vapor constant, temperature evaporation rate, respectively, substances f , i , g stand for liquid, number of channels, vapor phase, respectively.

When it comes to $t = t_2$, the local pressure in up channel overwhelming that of down channel, the bubble in up channel begins to expand, pushing the down bubble away from porous wall to let the fluid go through from down channel. In this way, pressures between different channels can exchange smoothly, fluid can always find some channels to flow through with no bubble blockage taking place.

Fig. 6 shows out-of-phase flow pattern inside two neighbouring bare channels along flow direction at run 40 with $G = 212 \text{ kg/m}^2\text{s}$, $q = 113.53 \text{ kW/m}^2$, $T_{in} = 92.87 \text{ }^\circ\text{C}$, $x_{out} = 0.065$. Numbering of channels can be seen in Fig. 1(b). In Fig. 6(a), bubble rushed into #4 bare channel from PFWA at $t = t_1$ ms when former bubble in #5 was blown downstream in the meantime. However, when it came to $t = t_1 + 1.0$ ms bubble run to #5 and former bubble in #4 was blown downstream. Fig. 6(a) illustrates bubbles injecting from PFWA to BCA alternatively within 1 ms. Fig. 6(b)-(d) show out-of-phase interface behaviours happened between #4 bare channel

and #5 bare channel at three locations ($A_2/A_3/A_4$) along flow direction. For example, in #4 channel near point A_2 , vapor core was “fat” at $t = t_2$ and then became “thin” at $t = t_2 + 1.0$ ms. But in #5 channel, vapor core was initially “thin” at $t = t_2$ and then became “thin” at $t = t_2 + 1.0$ ms. The variation of vapor core widths behaved out of phase property between neighbouring channels.

To get the quantitative analysis of bubble width oscillation, bubble confinement ratio η was defined as:

$$\eta = \frac{\text{vapor core width}}{\text{smooth channel width}} = \frac{w}{W} \quad (19)$$

The vapor core width was obtained manually by counting the number of pixels between up and down borders of a vapor core on the computer screen. The picture resolution was $3.64 \text{ } \mu\text{m/pixel}$ under present magnification. Definition of η in each channel was illustrated in Fig. 7(a), w_i is the vapor core width in channel # i . Transient bubble confinement ratios for channels #3 and #4 were showed in right side of Fig. 7(a) in black and red curves, respectively. By comparing the power spectrum distribution (PSD) of these two curves, one can find similar dominant frequencies of 1008.1 Hz and 917.7 Hz for channels #3 and #4, respectively. Fig. 7(b) magnifies the transient bubble confinement ratios in a narrow time span (9–16 ms). The bubble confinement ratios showed the spatial-time out-of-phase property quantitatively between two neighbouring bare channels. For example, when channel #3 reached maximum $\eta = w/W$, channel #4 reached minimum at $t_1 = 10.8$ ms; when channel #3 reached minimum $\eta = w/W$, channel #4 reached maximum at $t_2 = 11.6$ ms, highlighting the “spatial-reverse” feature. The variations of η vs time in each bare channel showed the “time-reverse” feature. Fig. 7(c) gives direct observations at above specific transient time.

3.3. Stable operation parameters

The high frequency interface oscillations (~ 1000 Hz) yielded overall stability. The responding time of measured parameters such as P_{in} (inlet pressures), T_{in} (fluid inlet temperatures), T_{out} (outlet temperatures) were ~ 10 ms order. It was impossible to trace oscillations of 1 ms. So high level of stabilities in typical cases of present study were shown in Fig. 8. $T_{w,ave}$ was obtained by averaging transient bottom-wall temperatures over the entail heater area (20.0 mm by 5.5 mm). Transient parameter variations of run 2 ($x_{out} = 0.02$, first row), run 9 ($x_{out} = 0.121$, second row) and run 12 ($x_{out} = 0.188$, third row) were illustrated in Fig. 8a-c respectively. Locations of T_w were chosen along flow direction covering single phase flow region (SP), onset of flow boiling region (ONB) and the two-phase flow region (TP), respectively. Since the recorded variation of P_{in} , T_{in} , and T_{out} was near the sensitivity of the measurement method, quantitative analysis was performed by adopting wall temperatures whose measurement sensitivity is $0.04 \text{ }^\circ\text{C}$. The standard deviation of wall temperature writes:

$$\sigma(X, Y) = \sqrt{\frac{1}{n-1} \sum_{i=1}^{n-1} (T_{X,Y}(t) - \bar{T}_{X,Y})^2} \quad (20)$$

where $T_{X,Y}(t)$ is the wall temperature at location (X, Y) and time t , $\bar{T}_{X,Y}$ is the time averaged temperature over sampling time, $n = 2500$ is the number of samples. The calculated values range of σ is $0.02 \text{ }^\circ\text{C}$ to $0.38 \text{ }^\circ\text{C}$. These above data show the function of gradient-porous walls in terms of stabilizing flow boiling parameters. It has been demonstrated that wall-temperature-oscillations amplitudes are inversely proportional to interface oscillations frequency [34]

$$T_w = T_{w,ave} + \frac{1}{f} \times \frac{q(W + W_{porous})l_{unit}S_n}{2\pi m_s C_{p,s}} \times (\cos(2\pi ft) - 1) \quad (21)$$

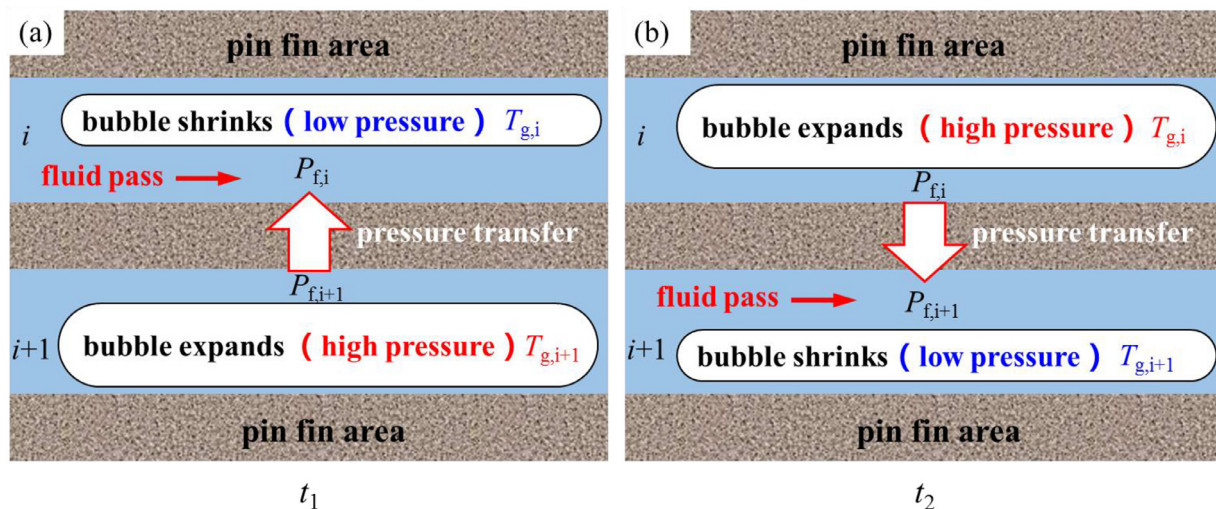


Fig. 5. Pressures delivering between two neighbouring bare channels.

As seen in Eq. (21), high frequency interface oscillation is the key to overall wall temperature stability. The wall temperature oscillation amplitude is inversely proportional to the oscillation frequency of bubble confinement ratio f . The higher the f , the more stable wall temperature is. For oscillation frequency $\sim 10^3 \text{ s}^{-1}$ as detected in present work, the oscillation amplitude value is in order of $10^{-2} \text{ }^\circ\text{C}$.

4. Thermal-hydraulic performance

4.1. Heat transfer process

4.1.1. Nucleate mechanism in PFWA

Bubbles prefer to nucleate in PFWA compared to BCA. This is because that large number of ideal nucleation cavities such as corners of solid pin fins in PFWA weakening the thermal non-equilibrium between vapor and liquid when the fluid is warmed up above saturated temperature. During bubble growing up period, there is a trend for bubbles to move from PFWA to the BCA, owing to surface energy gradients discussed in Section 3. Fresh liquid refills the space after the former bubbles leave, then bubble nucleation takes place again. The periodical formation and departure of bubbles in PFWA, followed by liquid rewetting, accounts for the nucleate heat transfer mechanism in PFWA. The surface energy gradients promote nucleate heat transfer by continuously driving bubbles away from PFWA.

4.1.2. Convective mechanism in BCA

In traditional solid wall microchannels, bubbles get expanded once they are triggered, quickly occupying channel, pushing nearby liquid up and down stream, then flushed by fresh liquid. These transient flow patterns account for the nucleate mechanism at low or moderate Bo cases. However, it is different in gradient porous wall microchannels: Because liquid mass exchange can be performed at channel width direction through PFWA, the bubble expansion induced over-pressure can be instantaneously transmitted to its neighbouring channels. So instead of occupying the whole channel after entering BCA, bubbles yield continuous annular flow even at low heat flux cases. Fast moving liquid film between vapor core and solid walls shows convective mechanism in BCA.

4.1.3. Hybrid heat transfer mechanism

When boiling number Bo is low. There are small numbers of cavities, indicating nucleate heat transfer in PFWA is weak. Little mass fluxes is transported from BCA to PFWA due to small

amount of bubble nucleation in PFWA. On the other hand, as a result of phase separation, bubble gathering in BCA, unconfined annular flow ensured strong convective heat transfer in BCA. This conclusion can be validated by Fig. 9. Fig. 9(a)(b) show wall temperatures and heat transfer coefficients in central axial line along flow direction for run 3, 17 and 48 respectively. Fig. 9(b) indicates the mass fluxes effects with the heat flux fixed around 38 kW/m^2 . Fig. 9(c)(d) illustrate situations of run 49,50 and 52, indicating heat fluxes effects on wall temperatures and heat transfer coefficients with mass flux around $247 \text{ kg/m}^2\text{s}$. Fig. 9(d) indicates heat flux effects with similar mass flux around $247 \text{ kg/m}^2\text{s}$. By comparing Fig. 9(b) and (d): Higher mass fluxes induce a slightly higher heat transfer coefficients at similar heat fluxes. While the heat fluxes have almost no effect on the heat transfer coefficients at similar mass flux. Thus, the competition of heat transfer in BCA and PFWA is confirmed: Neither heat fluxes nor mass fluxes have obvious influence on overall heat transfer coefficients.

As Bo number go to high level, high wall superheat temperatures extend the size ranges of nucleate cavities from micro meter to sub-micro meter or nano meter [51]. Large amounts of corners, defects of silicon pin-fin structure, usually have character length of less than $1 \text{ }\mu\text{m}$, gains more possibility for nucleation. The enlarged number of boiling cavities, increasing nucleate heat transfer in PFWA. However, higher heat fluxes generate more vapor, attracting more liquid move from BCA to PFWA, the decreased liquid mass fluxes weaken the whole convective heat transfer in BCA. As a result of such competition, overall heat transfer coefficients stay constant, being independent of both heat fluxes and mass fluxes. Fig. 10 shows cases at high Bo . Fig. 10(a)(b) show wall temperatures and heat transfer coefficients in central axial line for run 24 and 55 respectively. Fig. 10(b) indicate the mass fluxes effects with the heat fluxes fixed around 113 kW/m^2 . Fig. 10(c)(d) illustrate situations of run 53, 55 and 57, indicating heat fluxes effects with mass flux fixed around $249 \text{ kg/m}^2\text{s}$. Fig. 10(d) indicates heat flux effects with similar mass flux around $249 \text{ kg/m}^2\text{s}$. By comparing Fig. 10(b) and (d), heat-and-mass fluxes independent heat transfer coefficients are observed: Both heat and mass fluxes have almost no effect on the heat transfer coefficients. This gives evidence that hybrid heat transfer mechanism also dominates at high Bo number region.

4.1.4. Two-phase heat transfer at different Bo number

Widest range vapor quality can be found at channel exit, so investigation of heat transfer coefficients near channel outlet was

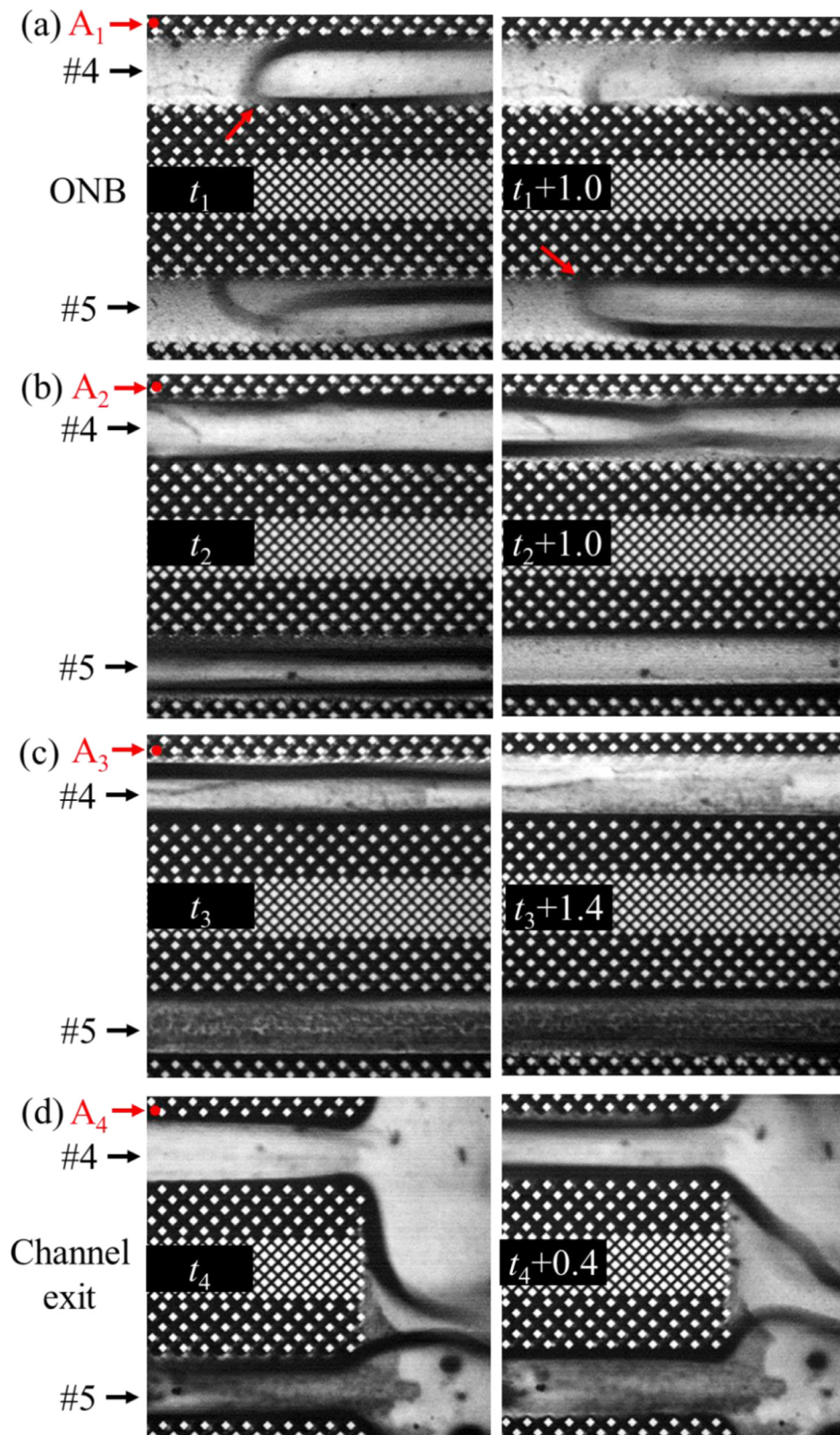


Fig. 6. Out of phase interface oscillations at different axial locations at run 40 with $G = 212 \text{ kg/m}^2\text{s}$, $q = 113.53 \text{ kW/m}^2$, $T_{\text{in}} = 92.87 \text{ }^\circ\text{C}$, $x_{\text{out}}=0.065$: a for location A_1 (7.5, 1.9); b for location A_2 (10, 1.9); c for location A_3 (15, 1.9); d for location A_4 (20,1.9) in unit of mm.

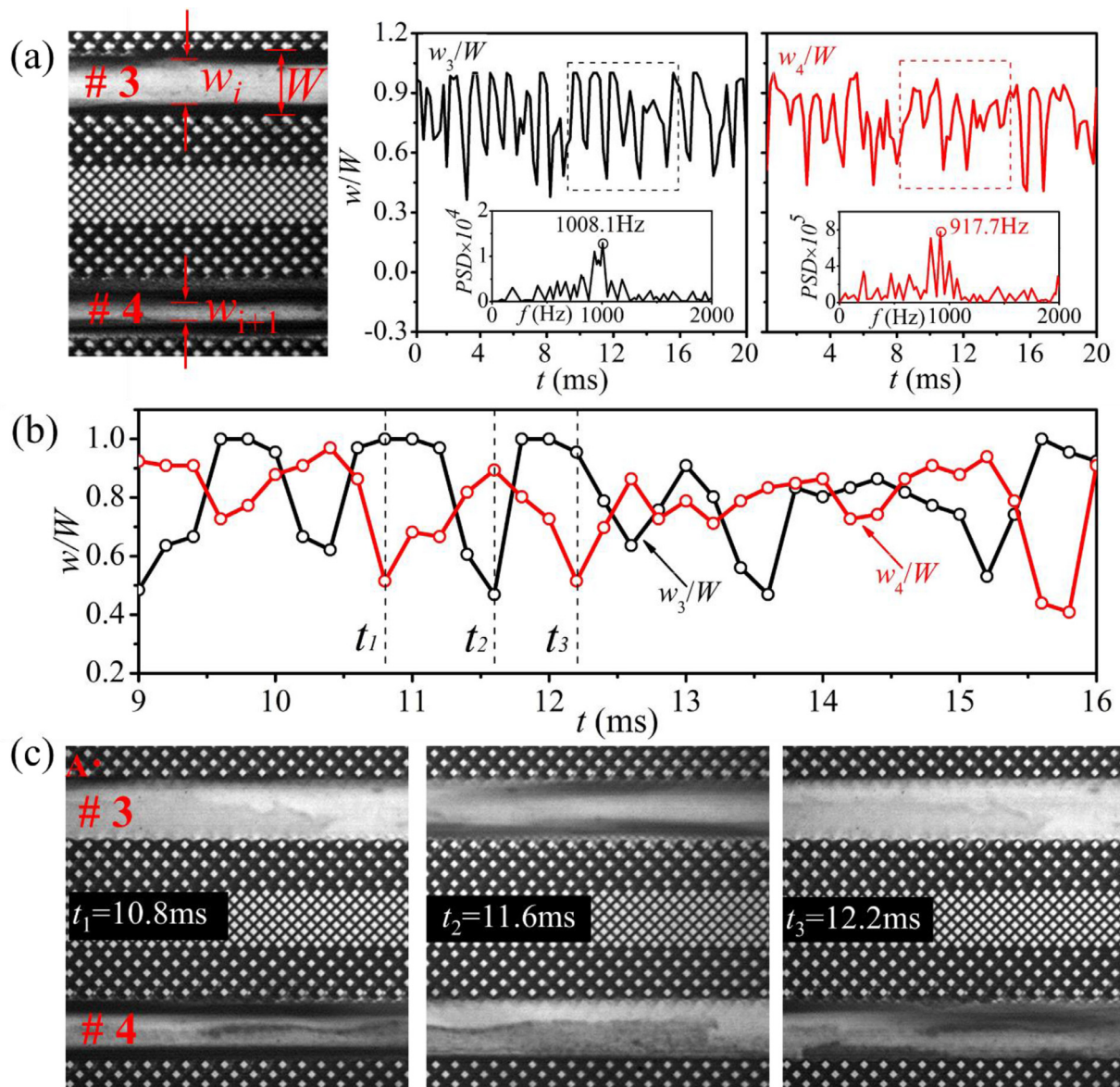


Fig. 7. Definition of bubble confinement ratio and its values versus time (at point A (15.0 mm, 1.4 mm), run 40 with $G = 212 \text{ kg/m}^2\text{s}$, $q = 113.53 \text{ kW/m}^2$, $T_{in} = 92.87 \text{ }^\circ\text{C}$ and $x_{out} = 0.065$).

often performed [52]. However, for present microchannel evaporator with inlet/outlet reservoirs, the measured wall temperature or heat transfer coefficients at channel exit location is influenced by axial heat conductivity from the end of microchannels to downstream reservoirs. To minimize conducting effect of reservoirs, a location ($X = 18 \text{ mm}$, $Y = 2.8 \text{ mm}$) near channel exit ($X = 20 \text{ mm}$, $Y = 2.8 \text{ mm}$) is chosen to investigate two phase heat transfer coefficients. Fig. 11 shows experimental results covering runs with parameters range of $q = 37.7\text{--}201.2 \text{ kW}$ and $G = 112.2\text{--}252.6 \text{ kg/m}^2\text{s}$. The values of Bo number cover 1 order of magnitude and two-phase heat transfer coefficients behave like “horizontal line”. This indicates that regardless of variation of G and/or q , the heat transfer coefficients remain unchanged. That is the result of competition of nucleate heat transfer in PFWA and convective heat transfer in BCA which will be further discussed in Section 4.2.

4.1.5. Heat transfer coefficients along flow direction in two phase regions

High-frequency interface oscillation results in high speed liquid rushing velocity in channel width direction v_y . When v_y is com-

parable to main fluid flow velocity v_x , the convective heat transfer in PFWA should be addressed because PFWA owns large amount of heat transfer areas. Fig. 12(a) indicates the local heat transfer coefficients along flow direction.

For a bubble confinement ratio oscillation with amplitude of A_m and dominating frequency of f , the average rushing velocity in channel width direction can be calculated as:

$$v_y = 4A_m f W \tag{22}$$

In present study,

$$A_m = \frac{(w/W)_{max} - (w/W)_{min}}{2} \tag{23}$$

which is determined experimentally. For example, at point ‘a’ where $X = 10 \text{ mm}$ showed in Fig. 12(a), $(w/W)_{max} = 0.80$, $(w/W)_{min} = 0.25$, $f = 708 \text{ Hz}$, $v_{y,a} = 4A_m f W = 0.128 \text{ m/s}$ (see left of Fig. 12(b)). Fig. 12(b)–(d) show confinement ratio oscillations in axial central line of channel #5 at point a ($X = 10 \text{ mm}$), point b ($X = 15 \text{ mm}$) and point c ($X = 20 \text{ mm}$) at run 40, respectively. Average confinement ratio $(w/W)_{ave}$ is increasing with higher local vapor mass quality. Visualization photos on the right hand

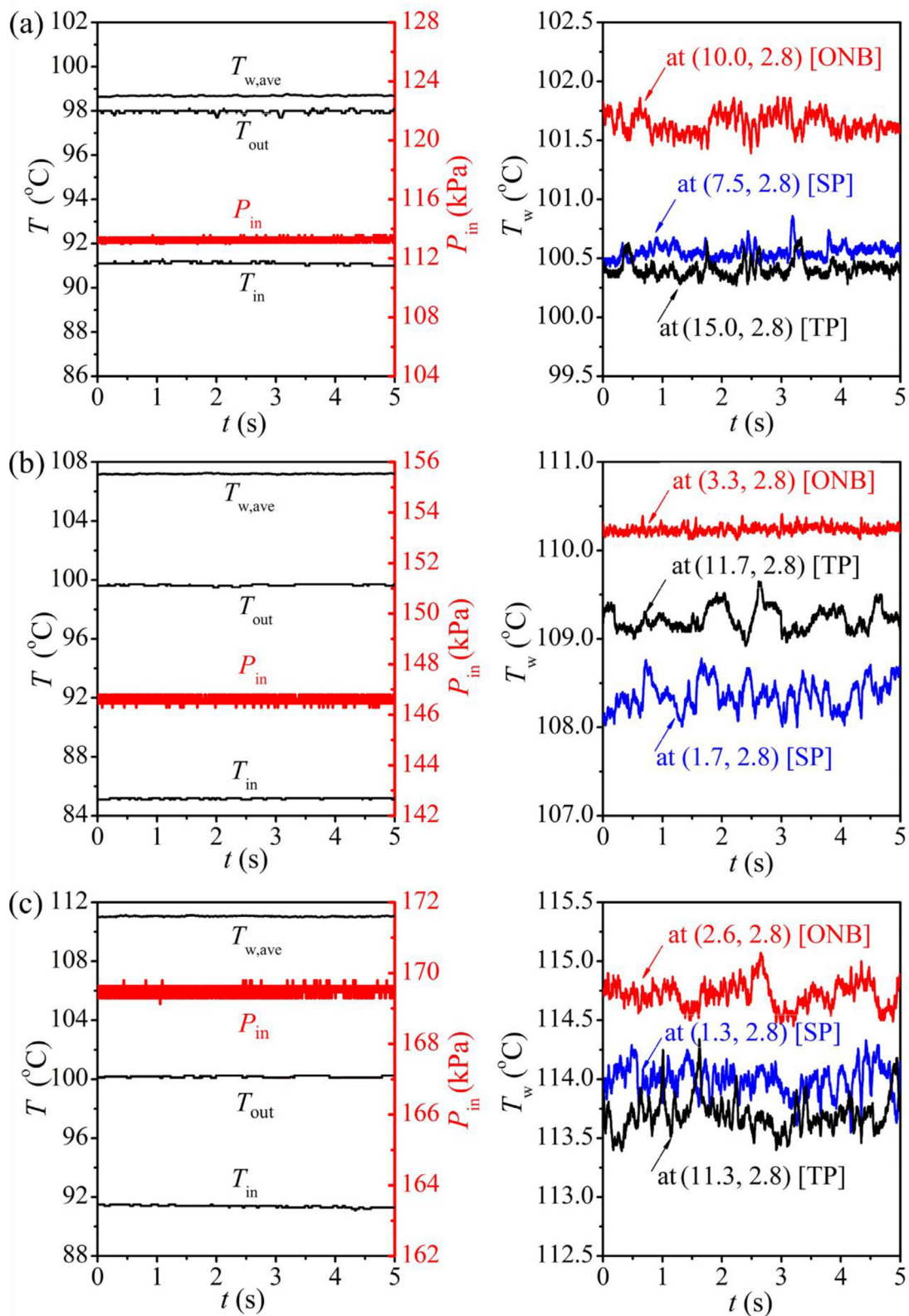


Fig. 8. Stable running parameters versus time (a for run 2 with $G = 113 \text{ kg/m}^2\text{s}$, $q = 27.93 \text{ kW/m}^2$, $T_{in} = 91.11 \text{ }^\circ\text{C}$, $x_{out}=0.020$; b for run 9 with $G = 112 \text{ kg/m}^2\text{s}$, $q = 115.45 \text{ kW/m}^2$, $T_{in}=85.17 \text{ }^\circ\text{C}$, $x_{out} = 0.121$; and c for run 12 with $G = 119 \text{ kg/m}^2\text{s}$, $q = 168.76 \text{ kW/m}^2$, $T_{in} = 91.38 \text{ }^\circ\text{C}$, $x_{out} = 0.188$).

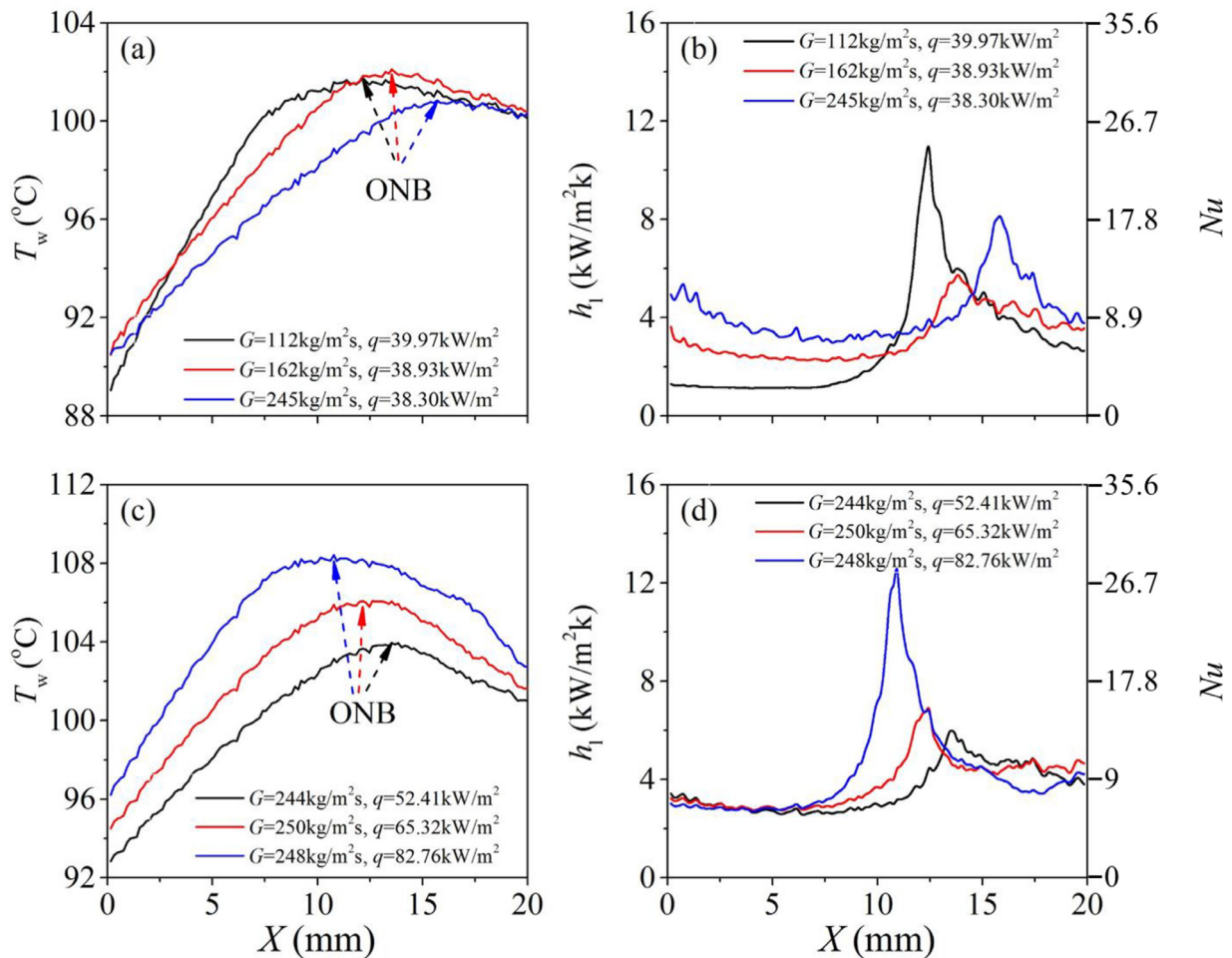


Fig. 9. Wall temperatures and heat transfer coefficients along flow direction at central line of the microchannels at low Bo number cases (a, b for runs 3 and 17 and 48; c, d for runs 49 and 50 and run 52).

shows evidently increase of average confinement ratio under increasing local vapor mass quality. In Fig. 12(b), where average local confinement ratio is lowest among those three points, the variation of confinement ratio is obvious, causing large $v_y=0.128$ m/s. In Fig. 12(c), where local average confinement ratio is relatively higher, the variation of confinement ratio is less obvious, causing smaller $v_y=0.067$ m/s. Fig. 12(d) illustrated situation near exit of channel, where local confinement ratio reaches highest with v_y being smallest. Decreased v_y means weaker convective heat transfer, resulting to decreased h_1 from point 'a' to point 'b' as showed in Fig. 12(a). The reason for rising of h_1 near exit of channel is axial heat conduct of bottom silicon base.

4.2. Heat transfer robustness and physical essentials

4.2.1. Thermal driving effect in gradient porous wall microchannels

At inlet of channels, as shown in Fig. 13(a) total mass flow rate $m_t=m_b+m_p$, where m_b and m_p are flow rate in bare channels and pin fin walls respectively. The existence of bubbles decreases mass flow rate in a certain channel but the whole mass flow rate remains unchanged as shown in Fig. 13(a)(b). As demonstrated in Section 3.1, a bubble emits from PFWA to BCA driven by surface energy gradient, during which process liquid fluid is propelled from BCA to PFWA by the growing bubble. In Fig. 13(c), assuming at $t = t_1$, a bubble was growing at the interface between BCA and PFWA. Pressure inside the bubble P_g is larger than the

pressure of surrounding bare-channel liquid P_b and pin-fin liquid P_p because of interface curvature. When it comes to $t = t_2$, the down part of bubble shrinks and the up part extends, making local pressure $P_b > P_p$. The liquid flows is thereby from P_b to P_p . Liquid flow from bare channel to pin-fin area, which is driven by growing bubbles from opposite direction, is called thermal driving effect of gradient porous wall. The thermal driving effect has two functions: a) reforming two-phase distribution in microchannels and b) pulling upstream flow in the BCA to the downstream of PFWA.

4.2.2. Variable mass flow rate in BCA along flow direction

In regular channels where mass exchange is forbidden between solid walls, mass flow rate along channels stay constant regardless of variation of heat fluxes or vapor fraction in a certain channel. However, in porous wall channels, mass fluxes in BCA is variable along flow direction. At small Bo number cases where two phase length l_{tp} is short, as shown in Fig. 13(d), collective effect of thermal driving effect is weak, less liquid is sucked into porous walls, so the outlet mass flow rate in BCA is larger. When the boiling number goes larger, longer two-phase length is expected in Fig. 13(e), more liquid goes into porous walls due to increasing collective effect of thermal driving effect. The outlet mass flow rate in BCA becomes smaller. The average mass fluxes in two-phase region is the space-average mass fluxes along channels. For bare channels with same inlet mass fluxes, the average mass fluxes at large Bo number cases are lower than that of small Bo number cases. In

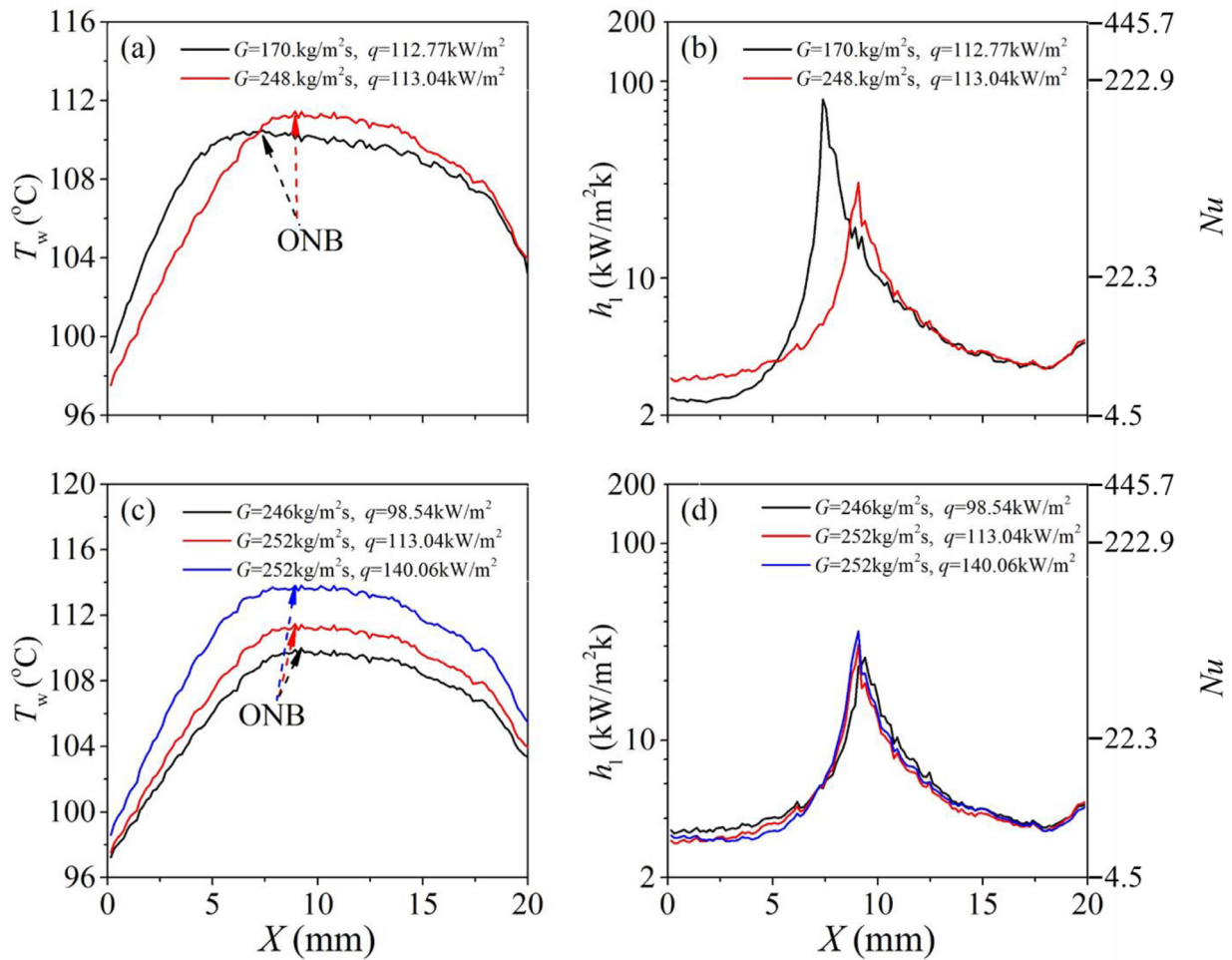


Fig. 10. Wall temperatures and heat transfer coefficients along flow direction at central line of the microchannels at high Bo number cases (a, b for runs 24 and 55; c, d for runs 53 and 55 and 57).

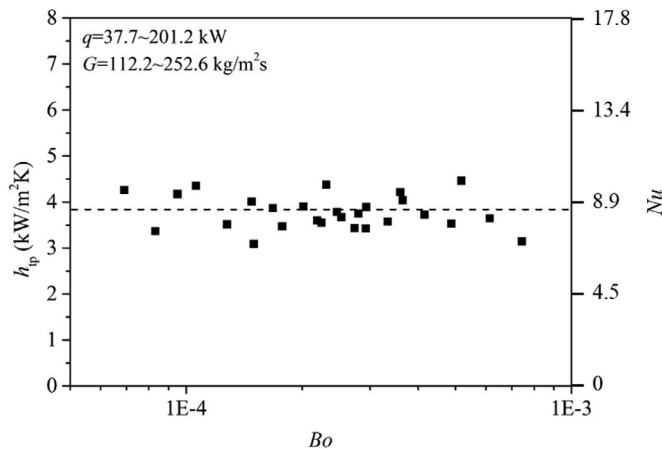


Fig. 11. Two-phase heat transfer with respect to Bo number at location (17.5, 2.8).

other words, the mass fluxes are higher in PFWA at larger Bo number cases because of stronger thermal driving effect.

4.2.3. Nucleate mechanism in PFWA vs convective mechanism in BCA

When Bo number is small, as discussed above, mass flow rate in BCA is large, causing strong convective heat transfer. On the other hand, nucleate heat transfer in PFWA is weak because of

small number of active nucleation caves. In addition, the wall superheat in PFWA is further decreased by strong convective heat transfer in BCA. So it is convective heat transfer overwhelming the nucleate heat transfer at small Bo cases. For large Bo number cases, however, the amount of liquid being sucked from BCA to PFWA due to thermal driving effect is large, the convective mechanism in BCA being suppressed. On the other hand, nucleate mechanism is reinforced because of high wall superheat under large Bo number cases. The thermal driving effect benefits for fresh liquid refilling from BCA to PFWA, supporting nucleate mechanism in PFWA. Therefore, the competition of heat transfer in BCA and PFWA makes global heat transfer coefficient insensitive to Bo number: One mechanism being strengthened while the other mechanism being weakened to achieve constant overall heat transfer coefficient, accounting for the robust heat transfer characteristics shown in Fig. 11.

4.3. Pressure drop

4.3.1. Phase-separation two-phase pressure drop reduction theory

For an isothermal system containing two-phase mixture of bubble and liquid, two-phase pressure drop is related to two items: (1) friction dissipation between liquid and bubble E_{lb} , and (2) friction dissipation between two phase flow and solid walls $E_{tp,w}$. By changing discontinuous phase from liquid drops to vapor bubbles described in [6], one can get flow boiling pressure drop gradient

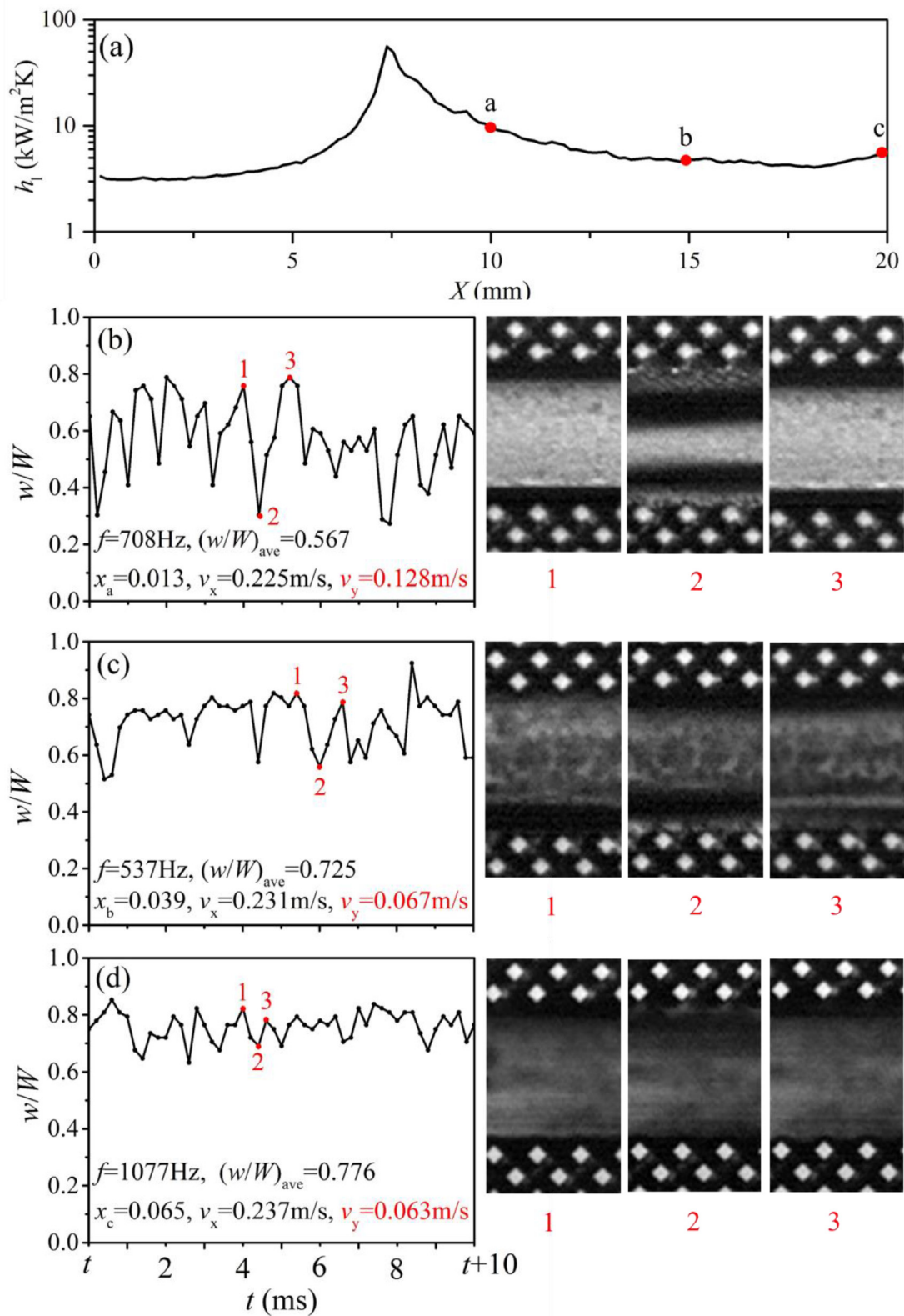


Fig. 12. Heat transfer coefficients along axial flow direction and bubble confinement ratios versus time (run 40 with $G = 212 \text{ kg/m}^2\text{s}$, $q = 113.53 \text{ kW/m}^2$, $T_{\text{in}} = 92.87 \text{ }^\circ\text{C}$, $x_{\text{out}} = 0.065$, point a, b and c have axial locations of $X = 10 \text{ mm}$, 15 mm and 20 mm , respectively).

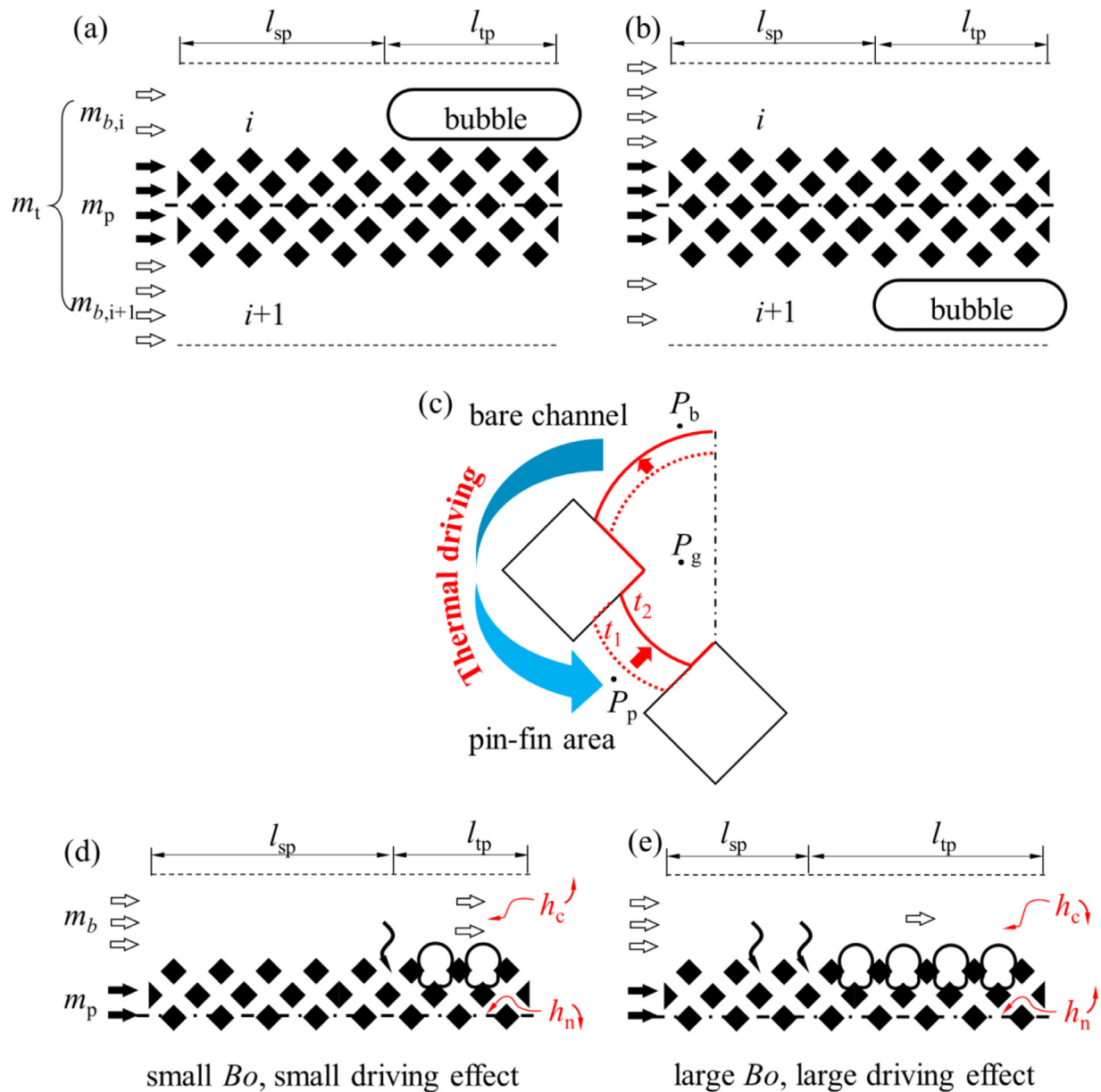


Fig. 13. Principle of heat and mass transfer under thermal driving effect (a, b for mass fluxes distribution along channel width direction, c for schematic of thermal driving effect, d,e for impact of Bo number on heat and mass transfer of BCA and PFWA, respectively).

along flow direction:

$$\frac{\Delta P}{L_c} = \frac{E_{lb} + E_{tp,w}}{A_p v_m L_c} = \frac{\frac{1}{8} C_d \rho_l v_s^2 v_b A_p a + \tau_{tp,w} \pi d_p v_m}{A_p v_m} \quad (24)$$

Where A_p is the channel cross sectional area. v_m is the velocity of two-phase mixture. L_c is the channel length. C_d is the drag coefficient of a vapor bubble in surrounding flowing liquid, ρ_l is the liquid density, v_s is the slip velocity between liquid and vapor bubble: $v_s = v_b - v_l$, v_b and v_l are the vapor bubble velocity and the liquid flow velocity, respectively. a is specific interface area of two-phase system. $\tau_{tp,w}$ is the shear stress between two-phase mixture and solid channel wall. d_p is the channel diameter. Eq. (24) tells us phase separation technology is helpful in reducing two-phase pressure drop because when small bubbles merge into continuous vapor phase, C_d and a are both decreased due to increasing bubble diameter in two-phase system, while other parameters is not related to bubble diameter. In fact, surface energy gradients merge small bubbles together to form big bubbles or

continuous annular flow. This process reforms vapor-liquid interface for a given void fraction, decreasing two-phase vapor-liquid interface areas and friction dissipation. Here, only frictional pressure drop was considered because the microchannel evaporator was horizontally placed. The pressure drops measurement points locate in the main flow pipe that are very closed to microchannels inlet/outlet (~1 mm). The diameter of main flow pipe (2 mm) is 20 times larger than the hydro diameter of present microchannels (~100 μm). Thus, the friction pressure drops in the main flow pipe between the measurement points can be neglected. Thus, we regard the measured pressure drop from differential pressure sensor as the two-phase pressure drop. The detailed calculation of local pressure drops can be seen in Eqs. (9) and (10).

4.3.2. Heat-flux dependent two-phase pressure drop in phase-separation microchannel evaporator

Fig. 14 shows very interesting relationships between two-phase pressure drops with heat/mass fluxes: In Fig. 14(a), pres-

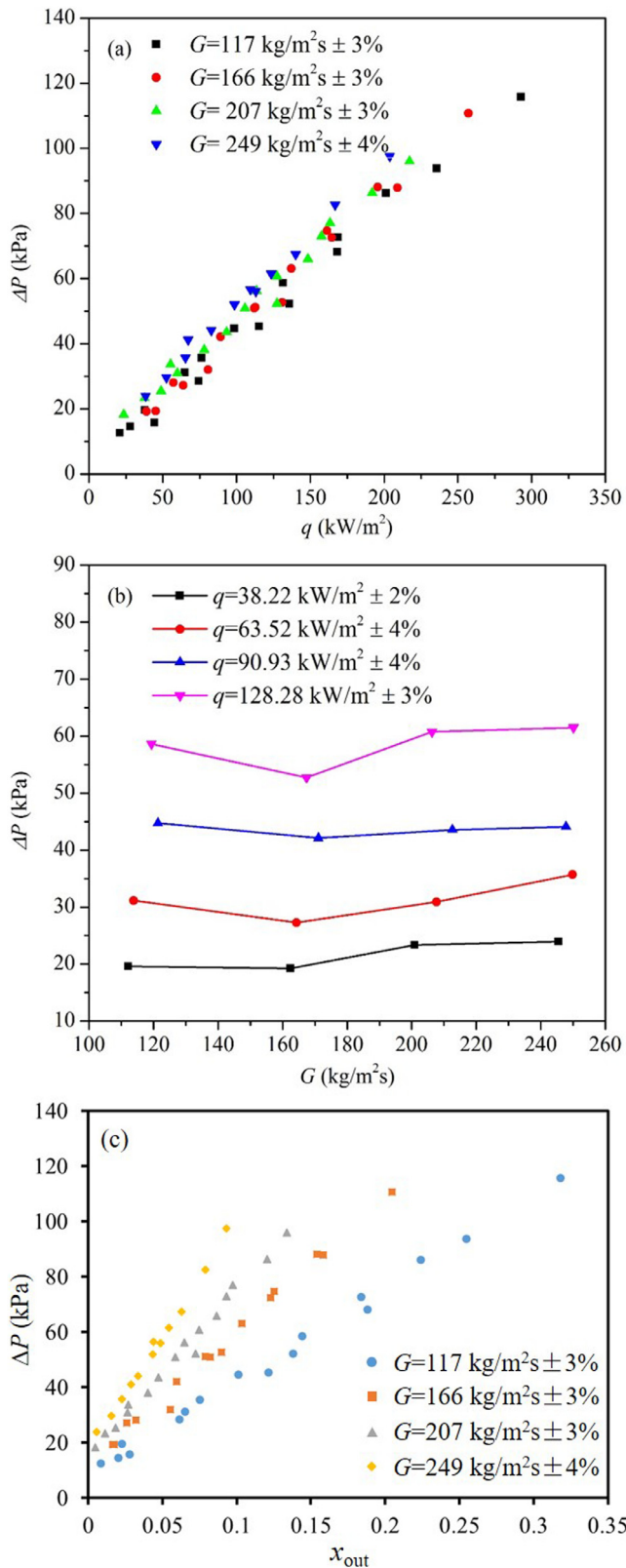


Fig. 14. Two phase pressure drop in phase separation microchannel showing insensitivity of G on $d\Delta P$ (a for channel pressure drops against heat fluxes at different mass fluxes, b for channel pressure drops against mass fluxes at different heat fluxes, c for pressure drops against outlet qualities).

sure drops of four groups of mass fluxes ranging from 117 kg/m²s to 249 kg/m²s are compared under different heat fluxes. Linear correlations are found between pressure drops and heat fluxes while the fluid mass fluxes have almost no effect on the pressure drop. This heat-flux-dependent-only property is clearly illustrated in Fig. 14(b) in which four groups of heat fluxes ranging from 38.22 kW/m² to 128.28 kW/m² curves are compared under different mass fluxes. Flat curves in each group of Fig. 14(b) show that pressure drops are insensitive to fluid mass fluxes under same heat fluxes. This unique dynamic characteristic is also a result of phase separation. Pressure drops mainly take place in two-phase region where vapor speed is much higher than liquid speed, causing most surface friction energy dissipation. Pressure drops in BCA owning most two-phase interface should be focused. According to energy balance, vapor producing rates is in liner relationship with heat fluxes. Most produced vapor are concentrated in BCA, determining two-phase pressure drops. So, heat fluxes have strong effect on pressure drops. The pressure drops are not sensitive to mass fluxes under similar heat fluxes for phase-separation evaporator. If we check the pressure drops against vapor qualities under four groups of mass fluxes ranging from 117 kg/m²s to 249 kg/m²s, as seen in Fig. 14(c), it is obvious that the pressure drops are larger under higher outlet vapor qualities for all the 4 groups of mass fluxes. This is because there is more vapor concentrated in BCA causing larger two-phase pressure drops as the vapor qualities are larger. Besides, under same outlet vapor qualities, the pressure drops are higher for larger mass fluxes.

5. Comments on the phase separation evaporator

Boiling heat transfer consists of two mechanisms of nucleation and convection, which are influenced by flow patterns. The link between heat transfer and flow patterns can be characterized by the Bo number [13]. Holding the phase separation evaporator within the Bo number in the range of 6.91×10^{-5} to 7.44×10^{-4} , heat transfer coefficients are not sensitive to heat fluxes at a given mass flux, ensuring flexible selection of running parameters. This finding is explained by defining two Bo numbers: $Bo_{PFWA} = q/(G_{PFWA}h_{fg})$ in porous wall region (PFWA) and $Bo_{BCA} = q/(G_{BCA}h_{fg})$ in bare channel region (BCA). Vapor concentrated in BCA suffering two-phase pressure drop, which is higher than single-phase pressure drop in PFWA. This leads to $G_{PFWA} > G_{BCA}$, noting that the vapor mass quality in PFWA is quite smaller than that in BCA, resulting in $Bo_{PFWA} < Bo_{BCA}$. This analysis concludes the nucleation mechanism in PFWA and convection mechanism in BCA, which are supported by the observed flow patterns (see Figs. 6 and 7).

The evaporator performance is competed by the two mechanisms in the two regions. When heat flux increases but mass flux keeps constant, the nucleation component in PFWA is enhanced. On the other hand, the enhanced bubble generation enhances the pumping effect from bare channel region to porous wall region. This reduces the mass flux in BCA to decrease the convection intensity there. The overall effect is to keep constant heat transfer coefficient at varied heating intensities (see Fig. 11).

Now we explain why pressure drop does not change at varied mass flow rates at a given heat flux. One notes that pressure drop is a function of both mass flux and vapor mass quality in a channel. When the total mass flow rate increases, the increased mass flow rate in bare channels gives rise to the reduced vapor mass quality, yielding the constant pressure drop. On the other hand, the increased mass flow rate in porous wall region weakens the bubble generation and release to yield the reduced vapor mass quality there, thus the pressure drop is not changed. The constant pressure drop can also be understood that it is caused by the self-assignment of the total flow rates in the two regions (see Fig. 14b).

In summary, by spatially population of pin-fin porous wall over the evaporator cross-section, we could decouple the two heat transfer mechanisms assigned in tow regions. The phase separation evaporator not only results in constant heat transfer coefficient at varied heat fluxes and/or mass flow rates, but also causes constant pressure drop at varied mass flow rates at a given heat flux, which are distinct to the conventional microchannels evaporator. These characteristics are benefit for the thermal management of heat transfer devices.

6. Conclusions

Phase separation evaporator concept was proposed: Gradient distributed micro pin fin arrays were used as phase separators. Boiling/evaporation heat and mass transfer in the evaporator with ultra-stable running parameters were investigated. Main conclusions of this study are drawn as follows:

- Decreased Gibbs free energy during bubble releasing from PFWA to BCA is the basic principle of microscale phase separation.
- A new hybrid heat transfer mechanism was discovered in phase separation evaporator. Competing of nucleate heat transfer in PFWA and convective heat transfer in BCA accounts for a stable overall heat transfer coefficient, ensuring predictable heat transfer.
- Physical principles and applications of thermal driving effect in the phase separation evaporator were analysed and discussed.
- Hydrodynamic demand curves in two-phase region was modified to “flat curve” without introducing extra restriction unit, eliminating static instability without sacrificing pressure drop.
- Advantages of phase separation evaporator over traditional solid wall microchannel evaporators were summarised.
- In the running parameters range, i.e. $P_{in}=110.57\sim 219.77$ kPa, $G = 112\sim 264$ kg/m²s, $q = 20.79\sim 292.82$ kW/m², $x_{out}=0.005\sim 0.318$, pressure drop is independent of mass flux for a given heat flux while the heat transfer is independent of Bo . It is recommended to test a wider range of running parameters such as higher heat fluxes and/or higher mass fluxes in the further research.

Declaration of Competing Interest

None.

CRediT authorship contribution statement

Xiongjiang Yu: Conceptualization, Investigation, Data curation, Visualization, Writing - original draft, Writing - review & editing, Project administration. **Jinliang Xu:** Conceptualization, Writing - review & editing, Supervision, Project administration, Funding acquisition. **Guohua Liu:** Writing - review & editing. **Xianbing Ji:** Writing - review & editing.

Acknowledgements

This work is supported by the National Natural Science Foundation of China (No. 51436004) and the National Natural Science Foundation of China (No. 51821004)

References

- [1] D.B. Tuckerman, R.F.W. Pease, High-performance heat sinking for VLSI, *IEEE Elec. Dev. Lett. EDL* 2 (1981) 126–129.
- [2] P. Rosa, T.G. Karayiannis, M.W. Collins, Single-phase heat transfer in microchannels: the importance of scaling effects, *Appl. Therm. Eng.* 29 (2009) 3447–3468.
- [3] N.H. Naqiuddin, L.H. Saw, M.C. Yew, F. Yusof, T.C. Ng, M.K. Yew, Overview of micro-channel design for high heat flux application, *Renew. Sust. Energ. Rev.* 82 (2018) 901–914.
- [4] J.A. Khan, A.K.M.M.M. Morshed, R. Fang, Towards Ultra-compact High Heat Flux Microchannel Heat Sink, *Procedia Eng.* 90 (2014) 11–24.
- [5] C.W. Wong, T.S. Zhao, Q. Ye, J.G. Liu, Transient Capillary Blocking in the Flow Field of a Micro-DMFC and Its Effect on Cell Performance, *J. Electrochem. Soc.* 152 (2005) A1600.
- [6] L. Cheng, Fundamental issues of critical heat flux phenomena during flow boiling in microscale-channels and nucleate pool boiling in confined spaces, *Heat Transf. Eng.* 34 (2013) 1016–1043.
- [7] X. Yu, J. Xu, J. Yuan, W. Zhang, Microscale phase separation condensers with varied cross sections of each fluid phase: heat transfer enhancement and pressure drop reduction, *Int. J. Heat Mass Transfer* 118 (2018) 439–454.
- [8] J.C. Chen, A correlation for boiling heat transfer to saturated fluids in convective flow, *Ind. Eng. Chem. Proc. Design Dev.* 5 (1966) 322–339.
- [9] H.J. Lee, S.Y. Lee, Heat transfer correlation for boiling flows in small rectangular horizontal channels with low aspect ratios, *Int. J. Multiphase Flow* 27 (2001) 2043–2062.
- [10] G. Hetsroni, A. Mosyak, Z. Segal, G. Ziskind, A uniform temperature heat sink for cooling of electronic devices, *Int. J. Heat Mass Transf.* 45 (2002) 3275–3286.
- [11] W. Qu, I. Mudawar, Flow boiling heat transfer in two-phase micro-channel heat sinks—I. Experimental investigation and assessment of correlation methods, *Int. J. Heat Mass Transfer* 46 (2003) 2755–2771.
- [12] S.G. Kandlikar, Heat transfer mechanisms during flow boiling in microchannels, *Trans ASME: J. Heat Transfer* 126 (2004) 8–16.
- [13] J. Xu, S. Shen, Y. Gan, Y. Li, W. Zhang, Q. Su, Transient flow pattern based microscale boiling heat transfer mechanisms, *J. Micromech. Microeng.* 15 (2005) 1344–1361.
- [14] A. Koşar, C.J. Kuo, Y. Peles, Boiling heat transfer in rectangular microchannels with reentrant cavities, *Int. J. Heat Mass Transfer* 48 (2005) 4867–4886.
- [15] B. Agostini, J.R. Thome, M. Fabbri, B. Michel, D. Calmi, U. Kloter, High heat flux flow boiling in silicon multi-microchannels – Part I: heat transfer characteristics of refrigerant R236fa, *Int. J. Heat Mass Transfer* 51 (2008) 5400–5414.
- [16] S.S. Bertsch, E.A. Groll, S.V. Garimella, Refrigerant flow boiling heat transfer in parallel microchannels as a function of local vapor quality, *Int. J. Heat Mass Transfer* 51 (2008) 4775–4787.
- [17] D. Deng, Y. Tang, D. Liang, H. He, S. Yang, Flow boiling characteristics in porous heat sink with reentrant microchannels, *Int. J. Heat Mass Transfer* 70 (2014) 463–477.
- [18] C. Falsetti, H. Jafarpoorchehab, M. Magnini, N. Borhani, J.R. Thome, Two-phase operational maps, pressure drop, and heat transfer for flow boiling of R236fa in a micro-pin fin evaporator, *Int. J. Heat Mass Transfer* 107 (2017) 805–819.
- [19] E.M. Fayyadh, M.M. Mahmoud, K. Sefiane, T.G. Karayiannis, Flow boiling heat transfer of R134a in multi microchannels, *Int. J. Heat Mass Transfer* 110 (2017) 422–436.
- [20] L. Cheng, G. Xia, Fundamental issues, mechanisms and models of flow boiling heat transfer in microscale channels, *Int. J. Heat Mass Transfer* 108 (2017) 97–127.
- [21] Y.K. Prajapati, P. Bhandari, Flow boiling instabilities in microchannels and their promising solutions – A review, *Exp. Therm. Fluid. Sci.* 88 (2017) 576–593.
- [22] J. Xu, J. Zhou, Y. Gan, Static and dynamic flow instability of a parallel microchannel heat sink at high heat fluxes, *Energ. Convers. Manage.* 46 (2005) 313–334.
- [23] J.R. Thome, Fundamentals of boiling and two-phase flows in microchannels, *International Heat Transfer Conference*, 13, Begel House Inc, 2006.
- [24] T. Zhang, T. Tong, J.-Y. Chang, Y. Peles, R. Prasher, M.K. Jensen, J.T. Wen, P. Phelan, Ledinegg instability in microchannels, *Int. J. Heat Mass Transfer* 52 (2009) 5661–5674.
- [25] S.G. Kandlikar, Nucleation characteristics and stability considerations during flow boiling in microchannels, *Exp. Therm. Fluid. Sci.* 30 (2006) 441–447.
- [26] P. Balasubramanian, S.G. Kandlikar, Experimental Study of Flow Patterns, Pressure Drop, and Flow Instabilities in Parallel Rectangular Minichannels, *Heat Transfer Eng.* 26 (2005) 20–27.
- [27] T. Zhang, J.T. Wen, Y. Peles, J. Catano, R. Zhou, M.K. Jensen, Two-phase refrigerant flow instability analysis and active control in transient electronics cooling systems, *Int. J. Multiphase Flow* 37 (2011) 84–97.
- [28] Y. Lv, G. Xia, L. Cheng, D. Ma, Experimental study on the pressure drop oscillation characteristics of the flow boiling instability with FC-72 in parallel rectangle microchannels, *Int. Commun. Heat Mass Transf.* 108 (2019) 104289.
- [29] A. Koşar, C.-J. Kuo, Y. Peles, Suppression of Boiling Flow Oscillations in Parallel Microchannels by Inlet Restrictors, *Trans ASME: J. Heat Transfer* 128 (2006) 251–260.
- [30] G. Wang, P. Cheng, A.E. Bergles, Effects of inlet/outlet configurations on flow boiling instability in parallel microchannels, *Int. J. Heat Mass Transfer* 51 (2008) 2267–2281.
- [31] S.G. Kandlikar, W.K. Kuan, D.A. Willistien, J. Borrelli, Stabilization of Flow Boiling in Microchannels Using Pressure Drop Elements and Fabricated Nucleation Sites, *Trans ASME: J. Heat Transfer* 128 (2006) 389–396.
- [32] C.T. Lu, C. Pan, Stabilization of flow boiling in microchannel heat sinks with a diverging cross-section design, *J. Micromech. Microeng.* 18 (2008) 075035.
- [33] J. Xu, G. Liu, W. Zhang, Q. Li, B. Wang, Seed bubbles stabilize flow and heat transfer in parallel microchannels, *Int. J. Multiphase Flow* 35 (2009) 773–790.
- [34] J. Xu, X. Yu, W. Jin, Porous-wall microchannels generate high frequency “eye-blinking” interface oscillation, yielding ultra-stable wall temperatures, *Int. J. Heat Mass Transfer* 101 (2016) 341–353.

- [35] G. Xia, Y. Lv, L. Cheng, D. Ma, Y. Jia, Experimental study and dynamic simulation of the continuous two-phase instable boiling in multiple parallel microchannels, *Int. J. Heat Mass Transfer* 138 (2019) 961–984.
- [36] H. Chen, J. Xu, Z. Li, F. Xing, J. Xie, W. Wang, W. Zhang, Flow pattern modulation in a horizontal tube by the passive phase separation concept, *Int. J. Multiphase Flow* 45 (2012) 12–23.
- [37] H. Chen, J. Xu, Z. Li, F. Xing, J. Xie, Stratified two-phase flow pattern modulation in a horizontal tube by the mesh pore cylinder surface, *Appl. Energ.* 112 (2013) 1283–1290.
- [38] Q. Chen, J. Xu, D. Sun, Z. Cao, J. Xie, F. Xing, Numerical simulation of the modulated flow pattern for vertical upflows by the phase separation concept, *Int. J. Multiphase Flow* 56 (2013) 105–118.
- [39] J. Xie, J. Xu, F. Xing, Z. Wang, H. Liu, The phase separation concept condensation heat transfer in horizontal tubes for low-grade energy utilization, *Energy* 69 (2014) 787–800.
- [40] J. Xu, B. An, D. Sun, The phase separation in a rectangular microchannel by micro-membrane, *Appl. Therm. Eng.* 88 (2015) 172–184.
- [41] J. Xu, X. Ji, W. Yang, Z. Zhao, Modulated porous wick evaporator for loop heat pipes: experiment, *Int. J. Heat Mass Transfer* 72 (2014) 163–176.
- [42] A. Jaikumar, S.G. Kandlikar, Enhanced pool boiling heat transfer mechanisms for selectively sintered open microchannels, *Int. J. Heat Mass Transfer* 88 (2015) 652–661.
- [43] A. Fazeli, M. Mortazavi, S. Moghaddam, Hierarchical biphilic micro/nanostructures for a new generation phase-change heat sink, *Appl. Therm. Eng.* 78 (2015) 380–386.
- [44] X. Dai, F. Yang, R. Fang, T. Yemame, J.A. Khan, C. Li, Enhanced single- and two-phase transport phenomena using flow separation in a microgap with copper woven mesh coatings, *Appl. Therm. Eng.* 54 (2013) 281–288.
- [45] L. Bai, L. Zhang, J. Guo, G. Lin, X. Bu, D. Wen, Evaporation/boiling heat transfer characteristics in an artery porous structure, *Appl. Therm. Eng.* 104 (2016) 587–595.
- [46] M. Dehghan, M.S. Valipour, S. Saedodin, Perturbation Analysis of the Local Thermal Non-equilibrium Condition in a Fluid-Saturated Porous Medium Bounded by an Iso-thermal Channel, *Transp Porous Media* 102 (2014) 139–152.
- [47] M. Dehghan, M.S. Valipour, S. Saedodin, Microchannels enhanced by porous materials: heat transfer enhancement or pressure drop increment? *Energy Convers. Manag.* 110 (2016) 22–32.
- [48] M. Dehghan, Y. Mahmoudi, M.S. Valipour, S. Saedodin, Combined Conduction–Convection–Radiation Heat Transfer of Slip Flow Inside a Micro-Channel Filled with a Porous Material, *Transp. Porous Media* 108 (2015) 413–436.
- [49] S. Rashidi, R. Masoodi, M. Bovand, M.S. Valipour, Numerical study of flow around and through a porous diamond cylinder in different apex angles, *Int. J. Numer. Methods Heat Fluid Flow* 24 (2014) 1504–1518.
- [50] J.P. Holman, W.J. Gajda, *Experimental Methods For Engineers*, Vol. 2, McGraw-Hill, New York, 2001.
- [51] X. Ji, J. Xu, H. Li, G. Huang, Switchable heat transfer mechanisms of nucleation and convection by wettability match of evaporator and condenser for heat pipes: nano-structured surface effect, *Nano Energy* 38 (2017) 313–325.
- [52] Y. Li, G. Xia, Y. Jia, Y. Cheng, J. Wang, Experimental investigation of flow boiling performance in microchannels with and without triangular cavities – A comparative study, *Int. J. Heat Mass Transfer* 108 (2017) 1511–1526.